Global changes in mRNA abundance drive differential shuttling of RNA binding proteins, linking cytoplasmic RNA degradation to transcription

Sarah Gilbertson[1], Joel D. Federspiel[2], Ella Hartenian[1], Ileana M. Cristea[2], and Britt Glaunsinger[1,3,4*]

[1]Department of Molecular and Cell Biology, University of California, Berkeley CA 94720-3370, [2]Department of Molecular Biology, Princeton University, Princeton, NJ 08544, [3]Department of Plant & Microbial Biology, University of California, Berkeley CA 94720-3370, [4]Howard Hughes Medical Institute.

*Correspondence: Glaunsinger@berkeley.edu

Summary

Alterations in global mRNA decay broadly impact upstream and downstream stages of gene expression, although signals that connect these processes are incompletely defined. Here, we used tandem mass tag labeling coupled with mass spectrometry to reveal that changing the mRNA decay landscape, as frequently occurs during viral infection, results in subcellular redistribution of RNA binding proteins (RBPs) in human cells. Accelerating Xrn1-dependent mRNA decay through expression of a gammaherpesviral endonuclease drove nuclear translocation of many RBPs, including poly(A) tail-associated proteins. Conversely, cells lacking Xrn1 exhibited changes in the localization or abundance of numerous factors linked to mRNA turnover. Using these data, we uncovered a new role for cytoplasmic poly(A) binding protein in repressing mammalian RNA polymerase II transcription upon its mRNA decay-induced translocation to the nucleus. Collectively, our results show that changes in cytoplasmic mRNA decay can directly impact protein localization, providing a mechanism to connect seemingly distal stages of gene expression.

Introduction

mRNA decay is a critical stage of gene expression that regulates the abundance and lifespan of cellular mRNAs. Many viruses including alpha and gammaherpesviruses, influenza A virus, and SARS coronavirus accelerate host mRNA degradation through the use of viral proteins that trigger endonucleolytic cleavage of mRNAs in the cytoplasm. Each of these viral proteins bypasses the rate-limiting deadenylation step of the basal decay pathway, resulting in cleaved mRNAs that are rapidly degraded by the major cellular 5’-3’ exonuclease Xrn1 (Covarrubias et al., 2011; Gaglia et al., 2012). This process, termed ‘host shutoff’, allows viruses to rapidly restrict cellular gene expression in order to blunt immune responses and liberate resources for

viral replication (Abernathy and Glaunsinger, 2015; Burgess and Mohr, 2015; Gaglia, 2010; Rivas et al., 2016). Viral endonucleases have also served as tools for deciphering how cells sense and respond to large changes in mRNA abundance.

While mRNA decay is often considered the terminal stage of gene expression, the rate of mRNA decay has recently been shown to influence transcription by RNA polymerase II (RNAPII) in both yeast and mammalian cells (Abernathy et al., 2015; Braun and Young, 2014; Haimovich et al., 2013; Sun et al., 2013). In yeast, a buffering system exists in which Xrn1 plays a major role in connecting mRNA synthesis and decay, presumably allowing cells to maintain an appropriate overall mRNA abundance. Mammalian cells also have a mechanism to sense mRNA levels, though the pathway appears to operate differently than in yeast. Here, accelerated cytoplasmic mRNA degradation does not lead to a compensatory increase in mRNA synthesis, as might be predicted by the homeostatic model, but instead broadly decreases cellular RNAPII transcription, thereby amplifying the restrictive gene expression environment (Abernathy et al., 2015).

This mRNA decay-transcription feedback pathway is activated in mammalian cells infected with gammaherpesviruses like Kaposi's sarcoma-associated herpesvirus (KSHV) and murine gammaherpesvirus 68 (MHV68), as well as upon expression of virally encoded mRNA endonucleases in uninfected cells. Herpesviral endonucleases, including the muSOX protein of MHV68, cleave mRNA but do not impact the abundance of noncoding RNAs transcribed by RNA polymerase I (RNAPI) or III (RNAPIII) (Covarrubias et al., 2011). Correspondingly, muSOX-induced mRNA decay elicits a significant decrease in RNA polymerase II (RNAPII) recruitment to cellular promoters (Abernathy et al., 2015). Notably, depletion of Xrn1 from muSOX-expressing cells prevents the ensuing RNAPII transcriptional repression. This suggests

that the initial mRNA cleavage and translational inactivation are insufficient to restrict transcription, and that subsequent exonucleolytic degradation of the cleaved mRNA fragments is a critical signaling step.

Little is currently known about this pathway linking cytoplasmic mRNA decay to RNAPII transcription in mammalian cells, including the nature of the signal that is transmitted between the two cellular compartments. An attractive hypothesis is that one or more RNA binding proteins (RBPs) differentially traffics between the cytoplasm and the nucleus when basal rates of mRNA decay are perturbed, thereby conveying global mRNA abundance information. Recent analyses indicate that mammalian cells contain hundreds of RBPs that bind polyadenylated mature mRNAs, and proteins within this group have been shown to regulate all stages of gene expression (Gerstberger et al., 2014; Mitchell and Parker, 2014; Müller-McNicoll and Neugebauer, 2013; Singh et al., 2015). Furthermore, RBPs frequently display nucleocytoplasmic shuttling behavior.

Here, we charted global alterations in protein localization that occur specifically in response to increased or decreased Xrn1 activity. This revealed a set of mammalian RBPs that preferentially move from the cytoplasm to the nucleus during accelerated mRNA decay, as well as components of the 5'-3' decay machinery and other RBPs whose subcellular distribution is altered in cells lacking Xrn1. Poly(A) tail associated proteins are overrepresented among the RBPs that accumulate in the nucleus under conditions of global mRNA decay, offering an explanation for how RNAPII could be selectively sensitive to mRNA abundance. Indeed, we uncovered a new role for cytoplasmic poly(A) binding protein (PABPC) in mediating mRNA decay-driven transcriptional repression. Our results reveal how mRNA levels exert significant influence on RBP localization and suggest that select RBPs transmit mRNA abundance

information from the cytoplasm to the nucleus to broadly influence gene expression, particularly under conditions of cellular stress.

Results

RNA binding proteins translocate from the cytoplasm to the nucleus in cells undergoing enhanced cytoplasmic mRNA decay

To chart mRNA decay-driven movement of proteins between the cytoplasm and the nucleus, we used a quantitative liquid chromatography/tandem mass spectrometry (LC/MS-MS)-based approach. Specifically, following subcellular fractionation, proteins from nuclear and cytoplasmic fractions were labeled with isobaric tandem mass tags (TMT). TMT labeling enables multiplexing of up to 11 samples per run and was proven to improve the analytical power for quantitation during viral infections (McAlister et al., 2012; PMJ et al., 2016). We used HEK293T cells expressing the MHV68 muSOX endonuclease to create a condition of accelerated, Xrn1-dependent cytoplasmic mRNA decay. We previously demonstrated that muSOX expression in these cells activates the mRNA decay-RNAPII transcription feedback pathway similar to virally infected fibroblasts (Abernathy et al., 2015). Pure populations of cells expressing either WT muSOX or the catalytically dead D219A muSOX point mutant were generated using Thy1.1-based cell sorting. Here, muSOX was fused to the cell surface glycoprotein Thy1.1 with an intervening self-cleaving 2A protease, causing release of Thy1.1 from muSOX for cell surface expression and selection. Three biological replicates of control, WT, and D219A muSOX expressing cells were then separated into nuclear and cytoplasmic fractions, and trypsin-digested proteins from each fraction were differentially TMT labeled prior to LC/MS-MS (**Figure 1A**).

Among the 5,994 total quantifiable nuclear proteins (detected in all replicates), 123 displayed significant nuclear enrichment (adjusted P value of ≤ 0.05) in WT muSOX expressing cells relative to the D219A mutant (**Figure 1B, Table S1-2**). We then removed from further analysis proteins that were simultaneously increased in the cytoplasm in muSOX expressing cells

to remove proteins that increase in overall abundance, as well as proteins displaying significant differences between the D219A catalytic mutant and the empty vector control. These filtering steps yielded a final list of 67 proteins that were differentially enriched in the nucleus under conditions of accelerated mRNA decay (**Figure 1B, Table S3**). Notably, 22 of the 67 proteins (33%) are annotated as RBPs (Pantherdb) in line with the expectation that mRNA-bound proteins in particular should be impacted during widespread mRNA degradation. In addition, 31 of the 67 proteins (46%) are listed as localized both to the cytoplasm and nucleus according to the Database for Annotation, Visualization and Integrated Discovery (DAVID), supporting the idea that they are shuttling factors. As an independent validation of these results, we evaluated 12 of the top hits by western blotting of fractionated cell lysates in control or muSOX-expressing cells, 10 of which recapitulated the MS results (**Figure S1A**).

Proteins associated with the poly(A) tail display robust mRNA decay-dependent nuclear translocation

The poly(A) tail is a defining mRNA feature and during basal mRNA decay, deadenylation is the initiating step that licenses subsequent decapping and exonucleolytic degradation of an mRNA (Schoenberg and Maquat, 2012). Thus, the binding state of poly(A) tail associated proteins could theoretically serve as a readout to distinguish the overall abundance of mRNA over other forms of RNA in the cytoplasm. Notably, nuclear relocalization of PABPC has been observed during infection with multiple viruses that promote mRNA decay, supporting the idea that poly(A) tail associated proteins may be particularly sensitive to mRNA abundance (Harb et al., 2008; Lee, 2009; Park et al., 2014; Piron et al., 1998; Salaun et al., 2010). Indeed, an overrepresentation analysis using Pantherdb revealed that poly(A) binding proteins, poly(U) binding proteins, and mRNA 3'UTR binding proteins were significantly overrepresented among

the 67 differentially expressed proteins (**Figure 1C, Figure S1B-C**). Proteins linked to the poly(A) tail consistently arose as robust hits in our MS dataset, including PABPC isoforms 1 and 4 (PABPC1, PABPC4), LA-related protein isoform 4 (LARP4), and heterogeneous nuclear ribonucleoprotein Q (HNRNPQ) (**Table S3**, **Figure 1D**). We confirmed that PABPC1 and LARP4 also translocate to the nucleus in NIH3T3 cells infected with WT MHV68, but not in cells infected with an MHV68 muSOX mutant virus (R443I) with impaired mRNA cleavage activity (Adler et al., 2000; Richner et al., 2011) (**Figure 1E**). Thus, poly(A) associated proteins preferentially move from the cytoplasm to the nucleus in response to muSOX-activated mRNA decay in both transiently transfected and virally infected cells.

Nuclear translocation of RNA binding proteins is dependent on mRNA degradation by Xrn1

Xrn1 is the major 5'-3' exonuclease in mammalian cells and is responsible for the degradation of 3' RNA fragments generated upon cleavage by muSOX (Gaglia et al., 2012). In the absence of Xrn1, the muSOX-induced transcriptional repression phenotype does not occur, suggesting that Xrn1 activity should be required for release and subsequent nuclear translocation of RBPs involved in decay-induced transcriptional repression (Abernathy et al., 2015). We therefore used Cas9-based genome editing to generate Xrn1 knockout clones in HEK293T cells and confirmed that muSOX expression in these cells failed to induce transcriptional repression (**Figure S2A-B**). Given that Xrn1 is a central component of the mammalian mRNA decay machinery, only low passage versions of these cells were used to decrease the likelihood of compensatory changes occurring in other decay components. Using the same TMT-LC/MS-MS strategy described above, we analyzed nuclear and cytoplasmic fractions from 3 biological replicates of Xrn1 knockout cells expressing muSOX or an empty vector control (**Figure 1A**).

Comparison of these data to the list of proteins from Table S3 indicated that 45 of the 67 hits failed to shuttle in muSOX-expressing Xrn1 knockout cells, confirming that our workflow identified factors that differentially shuttle in response to mRNA degradation (**Figure 2A, B)**.

Poly(A) tail degradation is normally carried out by deadenylases prior to activation of Xrn1-mediated decay from the 5' end, but we previously demonstrated that SOX-cleaved mRNAs are not deadenylated prior to their targeting by Xrn1 (Covarrubias et al., 2011). Indeed, analysis of endogenous PABPC1 and LARP4 localization by confocal microscopy and western blot analysis of fractionated cells confirmed that both proteins translocated from the cytoplasm to the nucleus upon muSOX expression in WT but not Xrn1 knockout cells (**Figure 2C-D, Figure S2C**).

Xrn1 knockout leads to subcellular redistribution of proteins functionally associated with RNA

Given that increased Xrn1 activity caused nuclear translocation of mRNA-associated RBPs, we hypothesized that RBPs linked to Xrn1 function might also exhibit altered subcellular distribution in cells lacking Xrn1. We first looked broadly for proteins with reproducibly altered abundance in the nucleus or the cytoplasm of Xrn1 knockout cells relative to the vector control cells. There were 149 and 158 proteins differentially expressed in the absence of Xrn1 in the nucleus or cytoplasm, respectively (adjusted P value ≤ 0.05) (**Figure 3A, Table S4**). Both the oligosaccharyltransferase (OST) complex and RBPs were significantly overrepresented among the set of differentially expressed proteins in each compartment (**Figure 3A, Figure S3).** The significance of the OST enrichment is currently unknown, although the OST complex has been shown to be critical for infection with flaviviruses, which depend on Xrn1 for the production of a subgenomic viral noncoding RNA (Chapman et al., 2014; Moon et al., 2012). However, the RBP

enrichment is in line with Xrn1 function, and it is notable that among the proteins significantly enriched in the nucleus of Xrn1 KO cells were factors that encompass the first steps of 5'-3' mRNA decay. These included all members of the decapping complex (DCP1A, DCP1B and DCP2), factors that promote decapping complex formation (EDC3 and EDC4), and a protein that connects the decapping complex to the deadenylation machinery (PATL1) (**Figure 3B**).

We next examined whether the absence of Xrn1 also impacted the relative abundance of its known interaction partners (as listed in the BioGRID database) in the two compartments (**Figure 3C**). This did not appear to be the case in the TMT data, as the majority of known Xrn1 protein partners were expressed at normal levels in the absence of Xrn1. However, there was a significant increase in the cytoplasmic levels of UPF1, a mediator of nonsense mediated mRNA decay (NMD). Conversely, PABPC4 levels were decreased in both compartments.

Finally, we considered the possibility that upon loss of Xrn1, cells might upregulate other components of the mRNA decay machinery. Perhaps surprisingly, out of all 5,994 detected proteins, only three were significantly upregulated in both the nucleus and the cytoplasm of Xrn1 knockout cells: GW182, Galectin-3, and BAG1. Among these, GW182 stands out because it is a member of the miRNA-induced silencing complex (miRISC) involved in recruitment of deadenylases to initiate degradation of target mRNAs (**Figure 3D**). This increase in GW182 abundance, along with the changes to DCP2, DDX6, and PABPC4, were independently validated by western blot analysis (**Figure 3E**). Collectively, these data suggest that there are not broad increases in cellular proteins in response to inhibition of 5'-3' mRNA decay. However, there appear to be selective increases in the nuclear levels of decapping-related proteins and the cytoplasmic level of UPF1, as well as a generalized enhancement of GW182 expression.

LARP4 shuttles to the nucleus in a PABPC-dependent manner

Protein relocalization in response to altered cytoplasmic mRNA decay could occur as a consequence of direct interactions with the nuclear transport machinery that are antagonized by mRNA, as has been documented for the PABPC nuclear localization signal (NLS) (Kumar et al., 2011). Alternatively, translocation could occur indirectly via interactions with other proteins that contain nuclear transport signals. To test for this latter possibility, we first plotted the network of known interactions among the list of proteins that relocalized in cells undergoing accelerated mRNA decay using the STRING database (**Figure 4A**). There were significantly more interactions among this set of proteins than would be predicted for a random group of proteins of similar size ($p = 0.0496$), with many of the interactions involving PABPC. This enrichment suggests that these proteins are biologically related, confirming what was seen in the GO term analysis. We examined the relocalization mechanism for one of the PABPC interacting proteins, LARP4 (Yang et al., 2011). We reasoned that if LARP4 relocalization involved direct interactions with the nuclear import machinery, then it should relocalize in muSOX-expressing cells in a PABPC independent manner. Conversely, if it was 'escorted' into the nucleus via its interaction with PABPC, then its relocalization should be blocked by PABPC depletion. Depletion of PABPC1 has been shown to lead to compensatory induction of the PABPC4 isoform, which can function in a redundant manner (Kumar, 2010). Therefore, we co-depleted both PABPC1 and PABPC4 using siRNAs. Upon co-depletion of the PABPC proteins, LARP4 no longer accumulated in the nucleus of muSOX-expressing cells (**Figure 4B**). In contrast, siRNA-mediated depletion of LARP4 had no effect on PABPC1 shuttling in these cells (**Figure 4C**). These results support a model in which LARP4 is brought into the nucleus in cells undergoing accelerated mRNA decay through its interaction with PABPC.

PABPC is required for the connection between mRNA decay and RNAPII transcription

Given the nuclear enrichment of many poly(A) and poly(U) associated proteins, we considered these factors to be strong candidates for involvement in the signaling pathway linking accelerated mRNA decay to RNAPII transcriptional repression. To determine if they were required for the mRNA decay-transcription feedback loop, we tested whether depletion of several of these factors individually altered RNAPII occupancy using chromatin immunoprecipitation assays (ChIP). To test the role of PABPC we co-depleted both PABPC1 and PABPC4 using siRNAs, then monitored RNAPII occupancy at two cellular promoters (*gapdh, rplp0*) previously shown to be responsive to mRNA decay-induced transcriptional repression (Abernathy et al., 2015). Compared to scramble siRNAs, depletion of PABPC1 and PABPC4 resulted in a restoration of RNAPII occupancy at the *gapdh* and *rplp0* promoters in muSOX expressing cells (**Figure 5A**). In contrast, RNAPII promoter occupancy remained repressed in muSOX expressing cells upon depletion of LARP4 (**Figure 5B**). In addition to poly(A) tail associated proteins, we tested the effects of depleting the poly(U) binding protein MSI1, as well as one of the transcriptional regulators that came out in the MS data, CHD3, on muSOX-induced transcriptional repression. However, RNAPII occupancy was not restored upon depletion of either of these proteins during muSOX-induced mRNA decay (**Figure S4A-B**). Taken together, these data suggest that PABPC is selectively required for RNAPII transcriptional repression during enhanced mRNA decay.

Nuclear accumulation of PABPC1 is sufficient to drive RNAPII transcriptional repression

Endogenous PABPC is subject to translational autoregulation, and our previous data suggested that the abundance of PABPC in uninfected cells is fine-tuned to match poly(A) tail availability (Kumar, 2010; Kumar et al., 2011). In this regard, even modest over-expression of PABPC1 leads to nuclear accumulation of the ‘excess’ (presumably non-poly(A) bound) protein

in cells lacking muSOX (**Figure 5C**). This feature enabled us to test whether nuclear accumulation of PABPC1 was sufficient to cause a reduction in RNAPII promoter recruitment in the absence of muSOX-induced mRNA decay. Indeed, FLAG-PABPC1 transfected cells displayed a significant decrease in RNAPII occupancy at the *gapdh and rplp0* promoters (**Figure 5D**). These observations suggested that the failure of muSOX to trigger transcriptional repression in Xrn1 knockout cells might be overcome by driving PABPC into the nucleus via overexpression. In agreement with this prediction, muSOX-induced transcriptional repression was restored in Xrn1 knockout cells upon transfection of FLAG-PABPC1, confirming that nuclear translocation of this RBP plays a central role in connecting cytoplasmic mRNA decay to RNAPII promoter recruitment (**Figure 5E**).

Discussion

Cellular mRNA abundance can be dramatically altered in response to a variety of pathogenic and nonpathogenic stresses including both viral and bacterial infections, and early apoptosis (Abernathy and Glaunsinger, 2015; Barry et al., 2017; Thomas et al., 2015). In many of these cases, accelerated cytoplasmic mRNA decay initiates a widespread reduction in transcript levels, often through the engagement of the major mammalian 5'-3' exonuclease Xrn1 (Covarrubias et al., 2011; Gaglia et al., 2012). In addition to altering the translational landscape, depletion of cytoplasmic mRNA elicits changes in upstream components of the mammalian gene expression pathway, including RNAPII transcription, largely by unknown mechanisms (Abernathy et al., 2015). Here, we tested the hypothesis that cellular RNA binding proteins may shift their subcellular localization in response to altered mRNA decay, thus conveying mRNA abundance information between the cytoplasm and the nucleus. Quantitative proteomics was previously reported to allow the discovery of viral infection-induced protein translocations (PMJ et al., 2017). Indeed, our unbiased TMT-based proteomics approach revealed that among the total cellular protein pool, an RBP-enriched protein subset concentrates in the nucleus specifically in response to increased mRNA decay in an Xrn1 dependent manner. RBPs have critical roles in all stages of gene expression (Müller-McNicoll and Neugebauer, 2013), and our data further emphasize their multifunctional capacity.

We also found that RBPs are enriched in the set of proteins with altered nuclear or cytoplasmic localization in Xrn1 knockout cells. Interestingly, factors involved in decapping, the event that directly precedes Xrn1 attack during basal mRNA decay, were selectively increased in the nuclei of cells lacking Xrn1. Furthermore, we detected increased levels of the NMD factor UPF1 in the cytoplasm and overall elevated levels of GW182 in these cells. One speculative

possibility is that these changes occur in response to cellular ‘reprogramming’ of the mRNA decay network, for example shifting emphasis towards 3’ end targeting mechanisms to compensate for the absence of the primary 5’ end decay mechanism. This scenario might explain the increase in GW182 levels, as it recruits the cellular deadenylase complexes PAN2-PAN3 and CCR4-NOT to mRNA targets to promote mRNA decay by Xrn1 (Braun et al., 2011; Chekulaeva et al., 2011; Fabian et al., 2011; Huntzinger and Izaurralde, 2011). In its absence, the increased GW182 levels may accelerate deadenylation to instead promote 3’-5’ decay. Alternatively, the RBP nuclear and/or cytoplasmic enrichment in Xrn1 knockout cells may reflect changes that occur when the cytoplasmic mRNA decay rate is reduced. The fact that we did not observe significant redistribution of the majority of Xrn1 interacting proteins argues against a model in which physical association with Xrn1 helps control decay factor protein localization.

Aside from RBPs, there was a clear overrepresentation of the OST complex, which catalyzes co-translational N-glycosylation, among the set of differentially expressed proteins in Xrn1 knockout cells. Although OST does not have established links to RNA decay or Xrn1, it has been shown to be a critical component of the replication cycle of flaviviruses such as Dengue and Zika (Marceau et al., 2016; Puschnik et al., 2017). Furthermore, these arthropod-borne flaviviruses inhibit Xrn1 activity through a subgenomic viral noncoding RNA that contains an Xrn1 blocking sequence (Chapman et al., 2014; Moon et al., 2012). In this context, it will be exciting to explore possible links between these two processes, especially given that small molecule OST inhibitors are now being tested for their pan-flaviviral inhibition (Puschnik et al., 2017).

Among the set of proteins that translocated in cells undergoing accelerated Xrn1-dependent mRNA decay, there was a striking enrichment in factors that bind the 3’end of

mRNAs. This supports the hypothesis that this class of RBPs would be significantly impacted by the mRNA abundance and availability. PABPC nuclear translocation in particular has been well documented in the context of infection with viruses that drive mRNA decay (Bablanian et al., 1991; Borah et al., 2012; Harb et al., 2008; Lee, 2009; Park et al., 2014; Piron et al., 1998; Salaun et al., 2010), and our unbiased proteomics approach establishes it as one of the most robustly relocalized RBPs under these conditions. Several features of PABPC render it an ideal indicator of mRNA abundance. First, its association with poly(A) tails implies that depletion of mRNAs but no other type of abundant non-polyadenylated RNAs should selectively alter the level of PABPC in the RNA bound versus unbound state. Second, nuclear import of PABPC is antagonized by cytoplasmic mRNA abundance. We previously reported that PABPC harbors noncanonical NLSs within its RNA recognition motifs (RRMs); upon poly(A) binding, these elements are masked and the protein is thus retained in the cytosol (Kumar et al., 2011). However, release of PABPC from mRNA exposes the NLSs, enabling its interaction with importin α and its subsequent nuclear import. The observation that PABPC localization is directly influenced by mRNA abundance suggest that cells must carefully calibrate the ratio of PABPC to mRNA. Indeed, PABPC protein binds an autoregulatory A-rich sequence in the 5'UTR of its own mRNA to disrupt 40S ribosomal scanning and reduce its translation (Neto et al., 1995; Wu and Bag, 1998).

When bound to poly(A) tails in the cytoplasm, PABPC contributes to mRNA stability and facilitates protein-protein interactions for efficient translation by the ribosome (Burgess and Gray, 2010; Fatscher et al., 2014). However, when concentrated in the nucleus, PABPC functions instead to restrict gene expression. One previously established mechanism by which gene expression is inhibited involves disruption of mRNA processing, where PABPC drives

hyperadenylation of nascent mRNAs (Kumar, 2010). Here, we reveal that nuclear PABPC can additionally repress transcription, as it is both necessary and sufficient to repress RNAPII promoter recruitment as a consequence of accelerated mRNA decay. Interestingly, the *S. cerevisiae* nuclear poly(A) binding protein Nab 2 has been shown to potentiate RNA polymerase III (RNAPIII) activity by directly binding RNAPIII and stabilizing TFIIIB with promoter DNA (Reuter et al., 2015), providing a precedent for PABPs influencing transcription. Thus far, we have not detected human PABPC associated with promoter DNA or with RNAPII (data not shown), suggesting that it may instead indirectly affect RNAPII recruitment, for example by impacting the function of other general transcription factors important for RNAPII promoter loading. Deciphering the mechanism by which PABPC represses RNAPII remains an important challenge for the future.

Although we did not detect a role for LARP4, MSI1, or CHD3 in RNAPII transcriptional repression, it is possible that additional translocated RBPs aside from PABPC may contribute to this phenotype. Alternatively, these proteins may engage in distinct gene regulatory functions in the nucleus. For example, a nuclear role for MSI1 has recently been uncovered during mouse spermatogenesis, when it translocates from the cytoplasm to the nucleus (Sutherland et al., 2015). In the cytoplasm, MSI1 negatively regulates the translation of its target RNAs by competing with eukaryotic initiation factor eIF4G for binding to PABPC (Kawahara et al., 2008). However, upon spermatocyte differentiation, MSI1 relocalizes to the nucleus through direct interaction with importin-5 (IPO5), where it concentrates at the silent XY chromatin domain. This not only releases its repression on translation, but also alters its repertoire of RNA targets in the nucleus. LARP4 also binds PABPC, but unlike MSI1, this interaction promotes mRNA poly(A) tail lengthening and stabilization in the cytoplasm (Yang et al., 2011). Our

findings suggest that nuclear accumulation of LARP4 is also dependent on its interaction with PABPC. LARP4 protein levels are controlled post-transcriptionally via an instability determinant within its coding sequence, suggesting that akin to PABPC, its protein abundance is tightly regulated (Mattijssen et al., 2017). The functions of LARP4 in the nucleus, as well as other RBPs identified in this work, are currently unknown. Exploring these roles and how they become manipulated during times of cellular stress are areas ripe for future studies.

Acknowledgements

This work was funded by NIH grant CA136367 to B.G., who is also an investigator of the Howard Hughes Medical Institute, and by NIH GM114141 to I.M.C. We thank all members of the Glaunsinger and Coscoy labs for helpful comments and suggestions.

Author Contributions

Conceptualization, S.G., B.G.; Methodology, J.D.F., I.M.C., S.G., B.G.; Validation, S.G., E.H.; Formal Analysis, S.G., J.F., I.M.C., B.G.; Investigation, S.G., J.F., E.H.; Writing – Original Draft, S.G.; Writing – Review & Editing, S.G., B.G., J.D.F., E.H., I.M.C.; Supervision, B.G., I.M.C.

Declaration of Interests

The authors declare no competing interests.

References

Abernathy, and Glaunsinger (2015). Emerging roles for RNA degradation in viral replication and antiviral defense. Virology 479, 600–608.

Abernathy, Gilbertson, Alla, and Glaunsinger (2015). Viral Nucleases Induce an mRNA

Degradation-Transcription Feedback Loop in Mammalian Cells. Cell Host & Microbe 18, 243–253.

Adler, Messerle, Wagner, and Koszinowski (2000). Cloning and Mutagenesis of the Murine Gammaherpesvirus 68 Genome as an Infectious Bacterial Artificial Chromosome. Journal of Virology 74, 6964–6974.

Bablanian, R., Goswami, S.K., Esteban, M., Banerjee, A.K., and Merrick, W.C. (1991). Mechanism of selective translation of vaccinia virus mRNAs: differential role of poly(A) and initiation factors in the translation of viral and cellular mRNAs. J. Virol. *65*, 4449–60.

Barry, Ingolia, and Vance (2017). Global analysis of gene expression reveals mRNA superinduction is required for the inducible immune response to a bacterial pathogen. ELife 6, e22707.

Borah, Nichols, Hassman, Kedes, and Steitz (2012). Tracking expression and subcellular localization of RNA and protein species using high-throughput single cell imaging flow cytometry. RNA 18, 1573–1579.

Braun, and Young (2014). Coupling mRNA Synthesis and Decay. Molecular and Cellular Biology 34, 4078–4087.

Braun, Huntzinger, Fauser, and Izaurralde (2011). GW182 proteins directly recruit cytoplasmic deadenylase complexes to miRNA targets. Molecular Cell 44, 120–33.

Burgess, H.M., and Gray, N.K. (2010). mRNA-specific regulation of translation by poly(A)-binding proteins. Biochem. Soc. Trans. *38*, 1517–22.

Burgess, and Mohr (2015). Cellular 5′-3′ mRNA Exonuclease Xrn1 Controls Double-Stranded RNA Accumulation and Anti-Viral Responses. Cell Host & Microbe 17, 332–344.

Chapman, Costantino, Rabe, Moon, Wilusz, Nix, and Kieft (2014). The Structural Basis of Pathogenic Subgenomic Flavivirus RNA (sfRNA) Production. Science 344, 307–310.

Chekulaeva, M., Mathys, H., Zipprich, J.T., Attig, J., Colic, M., Parker, R., and Filipowicz, W. (2011). miRNA repression involves GW182-mediated recruitment of CCR4-NOT through conserved W-containing motifs. Nat. Struct. Mol. Biol. *18*, 1218–26.

Covarrubias, Gaglia, Kumar, Wong, Jackson, and Glaunsinger (2011). Coordinated Destruction of Cellular Messages in Translation Complexes by the Gammaherpesvirus Host Shutoff Factor and the Mammalian Exonuclease Xrn1. PLoS Pathogens 7, e1002339.

Fabian, Cieplak, Frank, Morita, Green, kumar, Nagar, Yamamoto, Raught, Duchaine, et al.

(2011). miRNA-mediated deadenylation is orchestrated by GW182 through two conserved motifs that interact with CCR4–NOT. Nature Structural and Molecular Biology nsmb.2149.

Fatscher, T., Boehm, V., Weiche, B., and Gehring, N.H. (2014). The interaction of cytoplasmic poly(A)-binding protein with eukaryotic initiation factor 4G suppresses nonsense-mediated mRNA decay. RNA *20*, 1579–92.

Federspiel, J.D., & Cristea, I.M. (2018). Considerations for identifying endogenous protein complexes from tissue via immunoaffinity purification and quantitative mass spectrometry. Methods in Molecular Biology. (Under Review)

Gaglia, and Glaunsinger (2010). Viruses and the cellular RNA decay machinery. Wiley Interdisciplinary Reviews: RNA 1, 47–59.

Gaglia, Covarrubias, Wong, and Glaunsinger (2012). A Common Strategy for Host RNA Degradation by Divergent Viruses. Journal of Virology 86, 9527–9530.

Gerstberger, Hafner, and Tuschl (2014). A census of human RNA-binding proteins. Nature Reviews Genetics 15, 829–845.

Haimovich, Medina, Causse, Garber, Millán-Zambrano, Barkai, Chávez, Pérez-Ortín, Darzacq, and Choder (2013). Gene Expression Is Circular: Factors for mRNA Degradation Also Foster mRNA Synthesis. Cell 153, 1000–1011.

Harb, Becker, Vitour, Baron, Vende, Brown, Bolte, Arold, and Poncet (2008). Nuclear Localization of Cytoplasmic Poly(A)-Binding Protein upon Rotavirus Infection Involves the Interaction of NSP3 with eIF4G and RoXaN. Journal of Virology 82, 11283–11293.

Huntzinger, and Izaurralde (2011). Gene silencing by microRNAs: contributions of translational repression and mRNA decay. Nature Reviews. Genetics 12, 99–110.

Kawahara, Imai, Imataka, Tsujimoto, Matsumoto, and Okano (2008). Neural RNA-binding protein Musashi1 inhibits translation initiation by competing with eIF4G for PABP. The Journal of Cell Biology 181, 639–653.

Kumar, and Glaunsinger (2010). Nuclear Import of Cytoplasmic Poly(A) Binding Protein Restricts Gene Expression via Hyperadenylation and Nuclear Retention of mRNA. Molecular and Cellular Biology 30, 4996–5008.

Kumar, Shum, and Glaunsinger (2011). Importin α-Mediated Nuclear Import of Cytoplasmic Poly(A) Binding Protein Occurs as a Direct Consequence of Cytoplasmic mRNA Depletion. Molecular and Cellular Biology 31, 3113–3125.

Lee, and Glaunsinger (2009). Aberrant Herpesvirus-Induced Polyadenylation Correlates With

Cellular Messenger RNA Destruction. PLoS Biology 7, e1000107.

Marceau, Puschnik, Majzoub, Ooi, Brewer, Fuchs, Swaminathan, Mata, Elias, Sarnow, et al. (2016). Genetic dissection of Flaviviridae host factors through genome-scale CRISPR screens. Nature 535, 159–63.

Mattijssen, S., Arimbasseri, A., Iben, J., Gaidamakov, S., Lee, J., Hafner, M., and Maraia, R. (2017). LARP4 mRNA codon-tRNA match contributes to LARP4 activity for ribosomal protein mRNA poly(A) tail length protection. ELife 6, e28889.

McAlister, Huttlin, Haas, Ting, Jedrychowski, Rogers, Kuhn, Pike, Grothe, Blethrow, et al. (2012). Increasing the Multiplexing Capacity of TMTs Using Reporter Ion Isotopologues with Isobaric Masses. Analytical Chemistry 84, 7469–7478.

Mitchell, S.F., and Parker, R. (2014). Principles and properties of eukaryotic mRNPs. Mol. Cell *54*, 547–58.

Moon, Anderson, Kumagai, Wilusz, Akira, Khromykh, and Wilusz (2012). A noncoding RNA produced by arthropod-borne flaviviruses inhibits the cellular exoribonuclease XRN1 and alters host mRNA stability. RNA 18, 2029–2040.

Müller-McNicoll, and Neugebauer (2013). How cells get the message: dynamic assembly and function of mRNA–protein complexes. Nature Reviews Genetics 14, nrg3434.

Neto, O.P., Standart, N., and Sa, C. (1995). Autoregulation of poly (A)-binding protein synthesis in vitro. Nucleic Acids Research *23*, 2198–2205.

Park, El-Guindy, Heston, Lin, Yu, Nagy, Borah, Delecluse, Steitz, and Miller (2014). Nuclear Translocation and Regulation of Intranuclear Distribution of Cytoplasmic Poly(A)-Binding Protein Are Distinct Processes Mediated by Two Epstein Barr Virus Proteins. PLoS ONE 9, e92593.

Piron, Vende, Cohen, and Poncet (1998). Rotavirus RNA-binding protein NSP3 interacts with eIF4GI and evicts the poly(A) binding protein from eIF4F. The EMBO Journal 17, 5811–5821.

Jean Beltran, P.M., Mathias, R.A., and Cristea, I.M. (2016). A Portrait of the Human Organelle Proteome In Space and Time during Cytomegalovirus Infection. Cell Syst *3*, 361–373.e6.

Jean Beltran, P.M., Federspiel, J.D., Sheng, X., and Cristea, I.M. (2017). Proteomics and integrative omic approaches for understanding host-pathogen interactions and infectious diseases. Mol. Syst. Biol. *13*, 922.

Puschnik, Marceau, Ooi, Majzoub, Rinis, Contessa, and Carette (2017). A Small-Molecule Oligosaccharyltransferase Inhibitor with Pan-flaviviral Activity. Cell Reports 21, 3032–3039.

Reuter, Meinel, and Sträßer (2015). The poly(A)-binding protein Nab2 functions in RNA polymerase III transcription. Genes & Development 29, 1565–1575.

Richner, J., Clyde, K., Pezda, A., Cheng, B., Wang, T., Kumar, G., Covarrubias, S., Coscoy, L., and Glaunsinger, B. (2011). Global mRNA Degradation during Lytic Gammaherpesvirus Infection Contributes to Establishment of Viral Latency. Plos Pathog *7*, e1002150.

Rivas, H.G., Schmaling, S.K., and Gaglia, M.M. (2016). Shutoff of Host Gene Expression in Influenza A Virus and Herpesviruses: Similar Mechanisms and Common Themes. Viruses *8*, 102.

Salaun, MacDonald, Larralde, Howard, Lochtie, Burgess, Brook, Malik, Gray, and Graham (2010). Poly(A)-Binding Protein 1 Partially Relocalizes to the Nucleus during Herpes Simplex Virus Type 1 Infection in an ICP27-Independent Manner and Does Not Inhibit Virus Replication. Journal of Virology 84, 8539–8548.

Sauls, Greco, Wang, Zou, Villasmil, Qian, Cristea, and Conlon (2018). Initiating Events in Direct Cardiomyocyte Reprogramming. Cell Reports 22, 1913–1922.

Schoenberg, and Maquat (2012). Regulation of cytoplasmic mRNA decay. Nature Reviews Genetics 13, 246–259.

Singh, Pratt, Yeo, and Moore (2015). The Clothes Make the mRNA: Past and Present Trends in mRNP Fashion. Annual Review of Biochemistry 84, 325–354.

Sun, Schwalb, Pirkl, Maier, Schenk, Failmezger, Tresch, and Cramer (2013). Global Analysis of Eukaryotic mRNA Degradation Reveals Xrn1-Dependent Buffering of Transcript Levels. Molecular Cell 52, 52–62.

Sutherland, Sobinoff, Fraser, Redgrove, Davidson, Siddall, Koopman, Hime, and McLaughlin (2015). RNA binding protein Musashi-1 directly targets Msi2 and Erh during early testis germ cell development and interacts with IPO5 upon translocation to the nucleus. The FASEB Journal 29, 2759–2768.

Thomas, Liu, Whangbo, McCrossan, Sanborn, Basar, Walch, and Lieberman (2015). Apoptosis Triggers Specific, Rapid, and Global mRNA Decay with 3’ Uridylated Intermediates Degraded by DIS3L2. Cell Reports 11, 1079–89.

Vizcaíno, J.A., Deutsch, E.W., Wang, R., Csordas, A., Reisinger, F., Ríos, D., Dianes, J.A.A., Sun, Z., Farrah, T., Bandeira, N., et al. (2014). ProteomeXchange provides globally coordinated proteomics data submission and dissemination. Nat. Biotechnol. *32*, 223–6

Wu, and Bag (1998). Negative Control of the Poly(A)-binding Protein mRNA Translation Is Mediated by the Adenine-rich Region of Its 5′-Untranslated Region. Journal of Biological

Chemistry 273, 34535–34542.

Yang, Gaidamakov, Xie, Lee, Martino, Kozlov, Crawford, Russo, Conte, Gehring, et al. (2011). La-Related Protein 4 Binds Poly(A), Interacts with the Poly(A)-Binding Protein MLLE Domain via a Variant PAM2w Motif, and Can Promote mRNA Stability. Molecular and Cellular Biology 31, 542–556.

Figure Legends

Figure 1. RNA binding proteins are translocated from the cytoplasm to the nucleus in cells undergoing enhanced cytoplasmic mRNA decay. (A) Diagram depicting the experimental setup. (B) Venn diagram of nuclear proteins that are specifically and significantly ($p < 0.05$) enriched in muSOX-expressing cells compared to D219A-expressing cells that also show either no change or a decrease in cytoplasmic abundance. (C) Gene ontology molecular function overrepresentation analysis by Pantherdb, graphed according to their false discovery rate (FDR). (D) Graphs showing the nuclear and cytoplasmic distribution of poly(A) binding proteins from the TMT-MS data. Graphs display the mean with SEM of 3 biological replicates. (E) Western blot of nuclear, cytoplasmic, and whole cell fractions of NIH3T3 fibroblasts mock infected or infected with WT or R443I MHV68 for 24h. GAPDH and histone H3 serve as fractionation and loading controls. Quantification of the abundance of PABPC1 and LARP4 in the nuclear fractions is shown on the right.

Figure 2. Nuclear translocation of RNA binding proteins is dependent on mRNA degradation by Xrn1. (A) Pie chart showing the percent of shuttling proteins that fail to translocate in Xrn1 KO cells. (B) Heat map depicting the average nuclear abundance in WT or Xrn1 KO HEK293T cells of the 67 significantly shifted proteins in samples expressing muSOX

or D219A, relative to the empty vector control. (C) Western blots of nuclear, cytoplasmic, and whole cell fractions of WT (left panel) or Xrn1 KO (right panel) HEK293T cells transfected with the indicated plasmid. GAPDH and histone H3 serve as fractionation and loading controls. (D) Confocal microscopy of WT or Xrn1 KO HEK293T cells transfected with GFP or GFP-muSOX, showing signals for DAPI stained nuclei (blue), PABPC (red), GFP (green), and the merged images (overlay). Arrow heads point to representative GFP-muSOX expressing cells.

Figure 3. Xrn1 knockout leads to subcellular redistribution of proteins functionally associated with RNA. (A) The number of proteins that are differentially expressed in Xrn1 knockout (KO) cells from the nucleus (149) and the cytoplasm (158). Gene ontology molecular function overrepresentation analysis by Pantherdb is shown for each compartment, graphed according to their false discovery rate (FDR). (B) Graphs showing the nuclear and cytoplasmic distribution of decapping-related proteins from the TMT-LC/MS-MS data. Graphs display the mean with SEM of 3 biological replicates. (C) Heatmap depicting the Log_2 abundance ratio in Xrn1 KO HEK293T cells compared to WT HEK293T cells of proteins identified as Xrn1 interactors using the BioGRID database. Proteins with a significant difference in abundance between WT and Xrn1 KO are listed in red. (D) Graph of nuclear and cytoplasmic distribution of GW182 from the TMT-LC/MS-MS data. Graph displays the mean with SEM of 3 biological replicates. (E) Western blot of nuclear, cytoplasmic, and whole cell fractions of WT and Xrn1 KO HEK293T cells. GAPDH and histone H3 serve as fractionation and loading controls.

Figure 4. LARP4 translocates to the nucleus in a PABPC-dependent manner. (A) STRING network of reported protein-protein interactions between the 67 proteins that shuttle in muSOX-expressing cells. Medium and high confidence interactions are shown with thin and thick

connector lines, respectively. (B, C) Western blots of nuclear and cytoplasmic fractions of vector- or muSOX-transfected HEK293T cells treated with the indicated siRNA. GAPDH and histone H3 serve as fractionation and loading controls. Quantification of LARP4 and PABPC abundance in the nuclear fractions is shown below.

Figure 5. PABPC is required for the connection between mRNA decay and RNAPII transcription.

(A, B) HEK293T cells treated with siRNAs targeting PABPC1 and 4 (A), LARP4 (B), or non-targeting scramble siRNAs were subsequently transfected with either empty vector or muSOX, then subjected to chromatin immunoprecipitation (ChIP) using antibodies to RNAPII or IgG. Western blots showing protein levels of PABPC1, PABPC4, and Larp4 after siRNA depletion are shown in the lower panels, along with a GAPDH loading control. (C) Western blots of nuclear and cytoplasmic fractions of HEK293T cells transfected with an empty vector or a plasmid containing FLAG-PABPC1. GAPDH and histone H3 serve as fractionation and loading controls. (D) HEK293T cells transfected with either empty vector or FLAG-PABPC1 were subjected to ChIP using antibodies to RNAPII or IgG. (E) WT or Xrn1 KO HEK293T cells transfected with either empty vector or FLAG-PABPC1 alone or together with muSOX were subjected to ChIP using antibodies to RNAPII or IgG. Purified chromatin in each of the above experiments was quantified by qPCR. Western blots showing the levels of Xrn1 in WT or Xrn1KO HEK293Ts are shown, along with a GAPDH loading control. All graphs display individual biological replicates as dots, with the mean and SEM. Statistical significance was determined using Student's t test *$p < 0.05$ **$p < 0.005$ ***$p < 0.0005$

Materials and Methods

Plasmids

Primers used for cloning are listed in Table S5. MHV68 muSOX was cloned into the Gateway entry vector pDON207 (Invitrogen), and then transferred into the Gateway-compatible peGFP-C1 destination vector to generate GFP-muSOX. Thy1.1-muSOX was generated by Infusion cloning (Clontech) of Thy1.1 (CD90.1) followed by a self-cleaving 2A peptide from foot-and-mouth disease virus in place of GFP into the Nhe1 and SacII restriction enzyme sites of GFP-muSOX. The D219A muSOX triple alanine mutant was made using Quikchange site-directed mutagenesis (Agilent). Thy1.1-GFP was created with Infusion cloning to insert GFP back into the vector with the BamHI and EcoRI restriction enzyme sites to replace muSOX with GFP. pCDEF3-Flag-PABPC1 was described previously (Kumar, 2010). The Cas9 (lentiCas9-Blast) and sgRNA (lentiGuide-Puro) viral vectors were made as previously described (Sanjana et al., 2014; Shalem et al., 2014). The Xrn1 sgRNA was chosen using the Broad sgRNA design website (Doench et al., 2014).

Cells and transfections

NIH 3T3 cells and HEK293T cells were maintained in DMEM (Invitrogen) supplemented with 10% fetal bovine serum. DNA transfections were carried out in HEK293T cells at 70% confluency in 15cm plates with 25μg DNA using PolyJet (SignaGen) for 24h. For small interfering RNA (siRNA) transfections, HEK293T cells were transfected twice over 48h with 100μM siRNA using Lipofectomine RNAiMAX (Thermo Fisher), whereupon the cells were transfected with the indicated DNA plasmid for an additional 24h. Non-targeting scramble siRNAs, LARP4, MSI1, and CHD3 siRNAs were obtained from Dharmacon (Scramble: D-001206-13-50, LARP4: M-016523-00-0020, MSI1: M-011338-01-0010, CHD3: M-023015-01-

0020). PABPC1 and PABPC4 siRNAs have been previously described and are listed in Table S5. (Kumar, 2010; Lee, 2009).

The Xrn1 knockout clone and control Cas9-expressing cells were made by transducing HEK293T cells as previously described (Sanjana et al., 2014; Shalem et al., 2014). Briefly, lenti-Cas9-blast lentivirus was spinfected onto a monolayer of HEK293T cells, which were then incubated with 20μg/ml blasticidin to remove non-transduced cells. These Cas9-expressing HEK293T cells were then spinfected with lentivirus made from lentiGuide-Puro containing the Xrn1 sgRNA sequence and selected with 1μg/ml puromycin. The pool of Xrn1 knockout cells was then single-cell cloned in 96-well plates and individual clones were screened by western blot to determine knockout efficiency.

Pure populations of cells expressing muSOX were generated using the Miltenyi Biotec MACS cell separation system. HEK293T cells were transfected with either Thy1.1-GFP, Thy1.1-muSOX, or Thy1.1-muSOX D219A for 24h, whereupon cells were washed twice with PBS and cell pellets were resuspended in 95μl auto-MACS rinsing buffer supplemented with 0.5% FBS and incubated with 3μl anti-CD90.1 microbeads on ice for 10-15 min, and mixed by flicking the tube every 5 min. Cells were then magnetically separated according to the manufacturer's instructions. Thy1.1 positive cells were used in all downstream experiments unless otherwise stated.

Viruses and infections

The MHV68 bacterial artificial chromosome (BAC), and the construction of the R443I muSOX mutant were previously described (Adler et al., 2000; Richner et al., 2011). MHV68 was produced by transfecting NIH 3T3 cells in 6-well plates with 2.5μg BAC DNA using Mirus TransIT-X2 (Mirus Bio) for 24h, whereupon the cells were split into a 10cm dish and harvested

after 5-7 days, once all the cells were green and dead. Virus was amplified in NIH 3T12 cells and titered by plaque assay. Cells were infected with MHV68 at an MOI of 5 for 24h.

Immunofluorescence assays

Cells were plated on coverslips coated with 100ug/mL poly-L-lysine and transfected at 70% confluency with either GFP or GFP-muSOX for 24h. Transfected cells were fixed in 4% formaldehyde, permeabilized with ice-cold methanol, and incubated with blocking buffer [1% Triton X-100, 0.5% Tween-20, 3% Bovine Serum Albumin] prior to incubation with mouse monoclonal PABPC diluted 1:25 (Santa Cruz Biotechnologies, 10E10) or rabbit polyclonal LARP4 diluted 1:200 (Thermo Fisher) in blocking buffer at 4°C overnight, followed by incubation with Alexa Fluor 594-conjugated goat anti-mouse secondary antibody (Thermo Fisher, 1:1000) and DAPI (Pierce, 1:1000). Coverslips were mounted on slides using Vectashield hard-set mounting medium (VectorLabs) and imaged by confocal microscopy on a Zeiss LSM 710 AxioObserver microscope.

Fractionation

293T cells were fractionated using the REAP method (Nabbi and Riabowol, 2015). Briefly, cells were washed twice with ice-cold PBS and the cell pellet was lysed in 0.1% NP-40 PBS lysis buffer. The nuclei were then isolated by differential centrifugation at 10,000 x *g* for 10 sec and the supernatant retained as the cytoplasmic fraction. For western blotting, the nuclei were sonicated in 0.1% NP-40 PBS lysis buffer.

Cell lysis and protein digestion

WT Cas9-HEK293T cells were transfected with Thy1.1-GFP, Thy1.1-muSOX, or Thy1.1-muSOX D219A. Xrn1 knockout HEK293T cells were transfected with Thy1.1-GFP or Thy1.1-muSOX for 24h, followed by Thy1.1 separation. Separated cells were then fractionated

as described above, and nuclear pellets were snap-frozen in liquid nitrogen. Cytoplasmic fractions were concentrated using an Amicon ultra filtration unit with a molecular weight cutoff of 3kDa (Millipore) and exchanged into a 50mM NH_4HCO_3, 2% Deoxycholate buffer and then snap frozen in liquid nitrogen. The nuclear pellets were lysed in 200µL of 100mM Tris-HCl, pH 8.0, 4% SDS, 1mM EDTA preheated to 70°C. Cytoplasmic fractions were thawed and adjusted to 1% SDS with a 10% SDS solution. Complete lysis of samples was achieved via five successive rounds of heating at 95°C for 3 min followed by sonication for 10 sec in a cup horn sonicator set on 1 sec pulses at medium output. Protein amounts were assessed by BCA protein assay (Pierce) and 50 µg of protein from each sample was simultaneously reduced and alkylated with 20mM tris(2-carboxyethyl)phosphine (Pierce) and chloroacetamide respectively for 20 min at 70°C. Protein samples were then cleaned up by methanol-chloroform precipitation (Wessel et al., 1984; Federspiel and Cristea, 2018). LC-MS grade methanol, chloroform, and water (at a 4:1:3 ratio) were added to the sample with vortexing following each addition. The samples were spun at 2,000 × *g* for 5 min at room temperature and the top phase was removed. Three volumes of cold methanol were then added and the samples were spun at 9,000 × *g* for 2 min at 4°C. All liquid was removed and the protein pellets were washed with five volumes of cold methanol and then spun at 9,000 × *g* for 2 min at 4°C. All liquid was removed again and the dried protein pellets were resuspended in 50mM HEPES pH 8.5 at a 0.5µg/µL concentration. Trypsin (Pierce) was added at a 1:50 trypsin:protein ratio and the samples were incubated at 37°C overnight.

TMT labeling

Digested samples were concentrated by speed vac to one half the original volume prior to labeling and adjusted to 20% acetonitrile (ACN). All three biological replicates were labeled concurrently with a 10-plex TMT kit (Thermo Fisher Scientific) as in (Sauls et al., 2018). The

TMT reagents (0.8mg per channel) were dissolved in 42µL of anhydrous ACN and 14µL of this was added to each sample following the scheme in Figure 1A and allowed to react at RT for 1h. The labeling was quenched by the addition of hydroxylamine to a final 0.5% (v/v) concentration followed by incubation at RT for 15 min. Labeled peptides were pooled at equal peptide amounts thereby generating three 10-plex experiments, each of which was an individual biological replicate. An initial test mix for each replicate was analyzed, and the apparent peptide ratios were determined. Mixing ratios were adjusted using the information from the test mix to correct for sample losses and generate mixes with equal peptide amounts per channel.

Peptide fractionation

Pooled peptides were acidified and fractionated by 2D StageTip (Sauls et al., 2018). Peptides were first desalted via C18 StageTips to remove unreacted TMT reagent by washing the bound peptides with 5% ACN, 0.5% formic acid (FA) and then eluting the peptides in 70% ACN, 0.5% FA. The eluted peptides were then bound to SCX StageTips and eluted in four fractions with sequential elution (100µL) as follows: (1) 0.05 M ammonium formate/20% ACN, (2) 0.05 M ammonium acetate/20% ACN, (3) 0.05 M ammonium bicarbonate/20% ACN, and (4) 0.1% ammonium hydroxide/20% ACN. Each of these fractions were diluted 1:1 with 1% trifluoroacetic acid and further fractionated by SDB-RPS StageTips with sequential elution (50µL) into three fractions as follows: (1) 0.2 M ammonium formate/0.5% FA/60% ACN, (2) 0.2 M ammonium acetate/0.5% FA/60% ACN, (3) 5% ammonium hydroxide/80% ACN. The resulting 12 fractions for each 10-plex experiment were dried *in vacuo* and resuspended in 5µL of 1% FA, 1% ACN in water.

LC-MS/MS analysis

Peptides (2µL) were analyzed by LC-MS/MS using a Dionex Ultimate 3000 UPLC coupled online to an EASYSpray ion source and Q Exactive HF. Peptides were separated on an EASYSpray C18 column (75µm x 50cm) heated to 50°C using a linear gradient of 5% ACN to 42% ACN in 0.1% FA over 150min at a flow rate of 250nL/min and ionized at 1.7kv. MS/MS analysis was performed as follows: an MS1 scan was performed from 400 to 1800 m/z at 120,000 resolution with an automatic gain control (AGC) setting of 3e6 and a maximum injection time (MIT) of 30ms recorded in profile. The top 18 precursors were then selected for fragmentation and MS2 scans were acquired at a resolution of 60,000 with an AGC setting of 2e5, a MIT of 105ms, an isolation window of 0.8 m/z, a fixed first mass of 100 m/z, normalized collision energy of 34, intensity threshold of 1e5, peptide match set to preferred, and a dynamic exclusion of 45s recorded in profile.

Informatic analysis of TMT data

MS/MS data were analyzed by Proteome Discoverer (Thermo Fisher Scientific, v2.2.0.388). The nuclear channels (126-128C) and cytoplasmic channels (129N-131) were analyzed in separate Proteome Discoverer studies to not bias the quantitation due to the expected protein expression differences between these two compartments. The Spectrum Files RC node was utilized to perform post-acquisition mass recalibration and the recalibrated spectra were passed to Sequest HT where two successive rounds of searching were employed against a Uniprot human database appended with common contaminants (2016-04, 22,349 sequences). Both search rounds required 5ppm accuracy on the precursor and 0.02Da accuracy on the fragments and included static carbamidomethyl modifications to cysteine, static TMT additions to peptide N-termini and lysine residues, dynamic oxidation of methionine, dynamic deamidation of asparagine, and dynamic methionine loss and acetylation of protein n-termini. The first Sequest HT search was for fully

tryptic peptides only and any unmatched spectra were sent to a second Sequest HT search, which allowed semi-tryptic peptide matches. All matched spectra were scored by Percolator and reporter ion signal-to-noise (S/N) values were extracted (The et al., 2016). The resulting peptide spectrum matches were parsimoniously assembled into a set of identified peptide and protein identifications with a false discovery rate of less than 1% for both the peptide and protein level and at least 2 unique peptides identified per protein. TMT reporter ion quantification was performed for unique and razor peptides with an average S/N of at least 10 and a precursor co-isolation threshold of less than 30% which did not contain a variable modification. Reporter ion values were normalized to the total detected signal in each channel and protein abundances were calculated as the sum of all normalized reporter ion values for each channel in each protein. Missing values were input using the low abundance resampling algorithm. The reporter ion values for the empty vector WT samples (channels 126 and 129N) were set as 100 and the other channels were scaled to this value. Statistically differential proteins were assessed via a background based ANOVA analysis implemented in Proteome Discoverer. Proteins and associated TMT reporter ion abundances and adjusted p-values from the ANOVA analysis were exported to Excel for further analysis. The mass spectrometry proteomics data reported in this paper have been deposited at the ProteomeXchange Consortium via the PRIDE partner repository (Vizcaíno et al., 2014). The accession number is pending.

Gene Ontology analysis and informatic software used

Differential proteins (adjusted p-value ≤ 0.05) were analyzed via over representation analysis (www.pantherdb.org) for associated gene ontology enrichments (Mi et al., 2016). Example proteins of different classes, along with all heatmaps, were graphed in GraphPad Prism v7.

Western blotting

Nuclear, cytoplasmic, and whole cell lysates were quantified by Bradford assay and resolved by SDS-PAGE and western blotted with antibodies against PABPC (Cell Signaling, 1:1000), PABPC4 (Bethyl, 1:1000), LARP4 (Thermo Fisher, 1:1000), Gapdh (Abcam, 1:3000), Histone H3 (Cell Signaling, 1:2000), LYRIC (Abcam, 1:1000), RRBP1 (Bethyl, 1:1000), MSI1 (Abcam, 1:1000), Lin28b (Abcam, 1:1000), CHD3 (Cell Signaling, 1:1000), RPP20 (Novus, 1:1000), THOC6 (Life Technologies, 1:1000), PNN (Life Technologies, 1:1000), EXO4 (rabbit polyclonal produced using recombinant EXO4 with an MBP tag, 1:1000), NPM (Abcam, 1:1000), GW182 (Abcam, 1:1000), DDX6 (Bethyl, 1:1000), DCP2 (Bethyl, 1:1000).

Chromatin immunoprecipitation (ChIP)

ChIP was performed on 15 cm plates of HEK293T cells transfected twice 4 h apart with the indicated plasmid DNA. 24 h after the first transfection, cells were crosslinked in 1% formaldehyde in PBS for 10 min at room temperature, quenched in 0.125 M glycine, and washed twice with ice-cold PBS. Crosslinked cell pellets were mixed with 1 ml ice-cold ChIP lysis buffer (5mM PIPES pH 8.0, 85mM KCl, 0.5% NP-40) and incubated on ice for 10 min, whereupon the lysate was dounce homogenized to release nuclei and spun at 1.5 x *g* for 5 min at 4°C. Nuclei were then resuspended in 500 μl of nuclei lysis buffer (50mM Tris-HCl pH 8.0, 0.3% SDS, 10mM EDTA) and rotated for 10 min at 4°C followed by sonication using a QSonica Ultrasonicator with a cup horn set to 75 amps for 20 min total (5 min on, 5 min off). Chromatin was spun at 16,000 x *g* for 10 min at 4°C and the pellet was discarded. 100μl of chromatin was diluted 1:5 in ChIP dilution buffer (16.7 mM Tris-HCl pH 8.0, 1.1% Triton X-100, 1.2 mM EDTA, 167 mM NaCl) and incubated with 10 μg mouse monoclonal anti-RNAPII (BioLegend, 8WG16) or rabbit IgG (Fisher Scientific) overnight, whereupon samples were rotated with 20 μl

protein G dynabeads (Thermofisher) for 2 h at 4°C. Beads were washed with low salt immune complex (20 mM Tris pH 8.0, 1% Triton-x-100, 2 mM EDTA, 150 mM NaCl, 0.1% SDS), high salt immune complex (20 mM Tris pH 8.0, 1% Triton-x-100, 2 mM EDTA, 500 mM NaCl, 0.1% SDS), lithium chloride immune complex (10mM Tris pH 8.0, 0.25 M LiCl, 1% NP-40, 1% Deoxycholic acid, 1 mM EDTA), and Tris-EDTA for 5 min each at 4°C with rotation. DNA was eluted from the beads using 100 μl of elution buffer (150 mM NaCl, 50 μg/ml proteinase K) and incubated at 50°C for 2h, then 65°C overnight. DNA was purified using a Zymo Oligo Clean & Concentrator kit. Purified DNA was quantified by qPCR using iTaq Universal SYBR Mastermix (BioRad) with the indicated primers (Table S5). Each sample was normalized to its own input.

Supplementary Information

Figure S1 related to Figure 1. RNA binding proteins are translocated from the cytoplasm to the nucleus in cells undergoing enhanced mRNA decay. (A) Western blots of nuclear, cytoplasmic, and whole cell fractions of HEK293T cells transfected with either empty vector control, WT muSOX, or D219A muSOX. GAPDH and histone H3 serve as fractionation and loading controls. (B, C) Graphs showing poly(U) (B) and 3' UTR (C) binding protein distributions in the nucleus and cytoplasm from the TMT-LC/MS-MS data. Graphs display the mean with SEM of 3 biological replicates.

Figure S2 related to Figure 2. Nuclear translocation of RNA binding proteins is dependent on mRNA degradation by Xrn1. (A) Western blots showing the levels of Xrn1 or the GAPDH loading control in WT or Xrn1 KO HEK293T cells. (B) WT or Xrn1 KO HEK293T cells transfected with either empty vector or muSOX were subjected to ChIP using antibodies to

RNAPII or IgG. Purified chromatin was quantified by qPCR. Graphs display individual biological replicates as dots, with the mean and SEM. Statistical significance was determined using Student's t test *p <0.05 **p <0.005 ***p <0.0005. (B) Confocal microscopy of WT or Xrn1 KO HEK293T cells transfected with GFP or GFP-muSOX, showing signals for DAPI stained nuclei (blue), LARP4 (red), GFP (green), and the merged images (overlay). Arrow heads point to representative GFP-muSOX expressing cells.

Figure S3 related to Figure 3. Xrn1 knockout leads to subcellular redistribution of proteins functionally associated with RNA. (A) Graphs showing the distribution of proteins of the oligosaccharyltransferase (OST) complex in the nucleus and cytoplasm from the TMT-LC/MS-MS data. Graphs display the mean with SEM of 3 biological replicates.

Figure S4 related to Figure 5. PABPC is required for the connection between cytoplasmic mRNA decay and RNAPII transcription. (A, B) HEK293T cells were treated with siRNAs targeting CHD3 (A), or MSI1 (B), or non-targeting scramble siRNAs, then transfected with either empty vector or muSOX and subjected to chromatin immunoprecipitation (ChIP) using antibodies to RNAPII or IgG. Purified chromatin was quantified by qPCR. Western blots showing the levels of CHD3 and MSI1 after siRNA depletion, along with a GAPDH or histone H3 loading control are shown below. Graphs display individual biological replicates as dots, with the mean and SEM. Statistical significance was determined using Student's t test *p <0.05 **p <0.005 ***p <0.0005.

Table S1. Nuclear proteome. Identified and quantified proteins in the nuclear fraction with associated TMT abundance values.

Table S2. Cytoplasmic proteome. Identified and quantified proteins in the cytoplasmic fraction with associated TMT abundance values.

Table S3. Proteins enriched in the nucleus in muSOX expressing cells. Proteins significantly ($p < 0.05$) enriched in the nucleus in muSOX expressing cells compared to D219A expressing cells that also show either no change or a decrease in cytoplasmic abundance. Listed from left to right: Accession number, gene symbol, nuclear abundance ratio, muSOX compared to D219A muSOX, subcellular localization, and gene ontology (GO) Molecular Function. The Database for Annotation, Visualization, and Integrated Discovery (DAVID v6.8) was used for subcellular localization and GO molecular function information.

Table S4. Proteins differentially expressed in Xrn1 knockout cells. Proteins that are differentially expressed in Xrn1 knockout cells in the nucleus (left) and the cytoplasm (right). Listed are the protein accession numbers and the corresponding gene symbol.

Table S5. Primer and custom siRNA sequences.

Figure 1

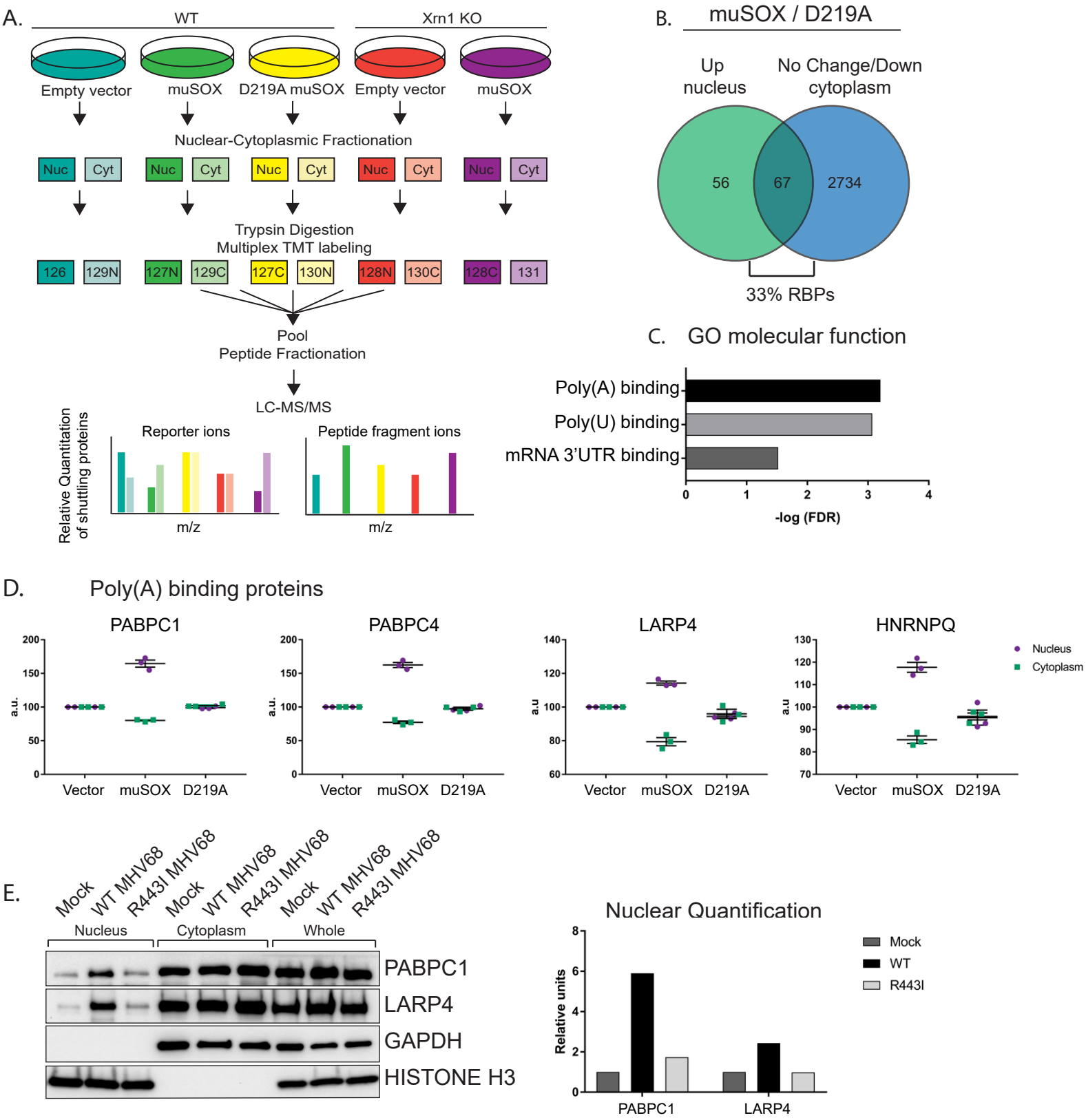

Figure 1. RNA binding proteins are translocated from the cytoplasm to the nucleus in cells undergoing enhanced cytoplasmic mRNA decay. (A) Diagram depicting the experimental setup. (B) Venn diagram of nuclear proteins that are specifically and significantly ($p < 0.05$) enriched in muSOX-expressing cells compared to D219A-expressing cells that also show either no change or a decrease in cytoplasmic abundance. (C) Gene ontology molecular function overrepresentation analysis by Pantherdb, graphed according to their false discovery rate (FDR). (D) Graphs showing the nuclear and cytoplasmic distribution of poly(A) binding proteins from the TMT-MS data. Graphs display the mean with SEM of 3 biological replicates. (E) Western blot of nuclear, cytoplasmic, and whole cell fractions of NIH3T3 fibroblasts mock infected or infected with WT or R443I MHV68 for 24h. GAPDH and histone H3 serve as fractionation and loading controls. Quantification of the abundance of PABPC1 and LARP4 in the nuclear fractions is shown on the right.

Figure 2

A. Xrn1 requirement for shuttling

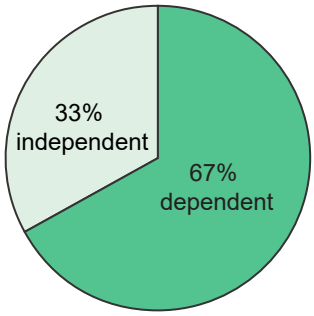

B.

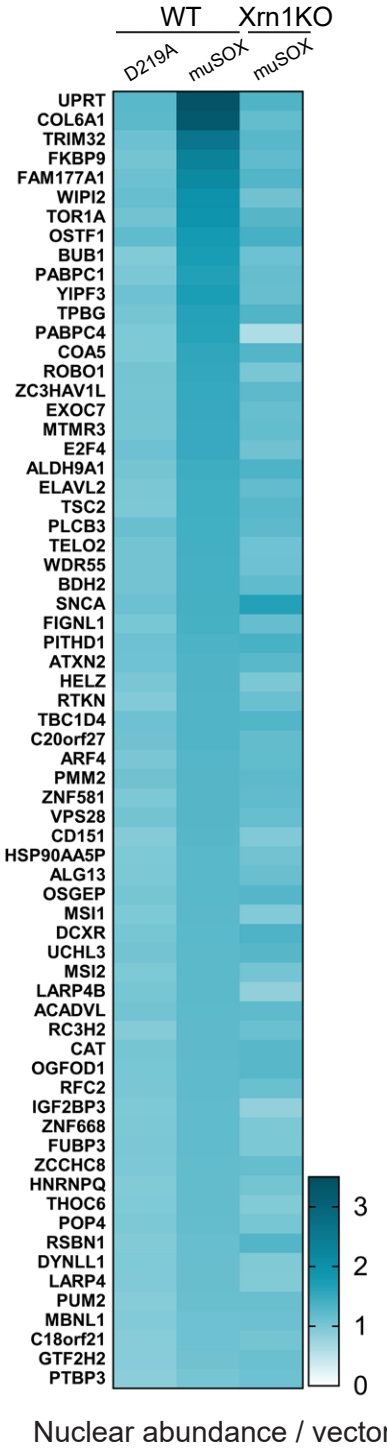

C.

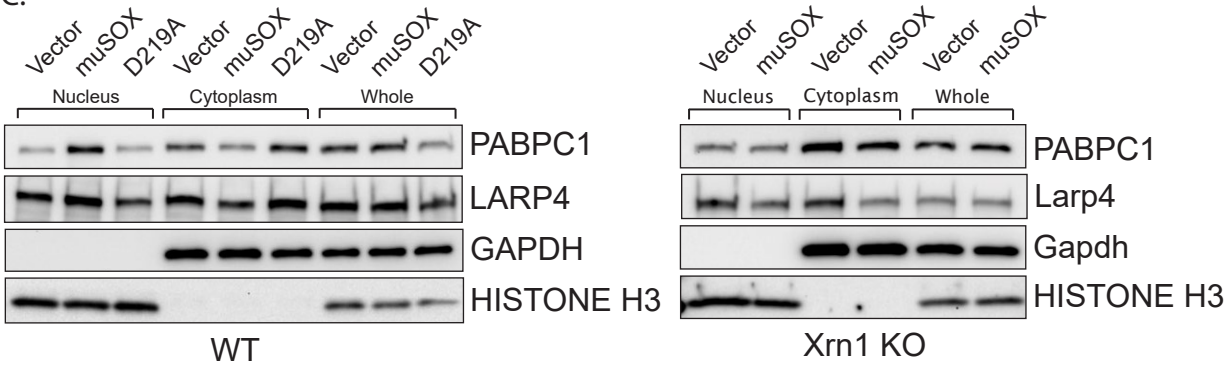

D.

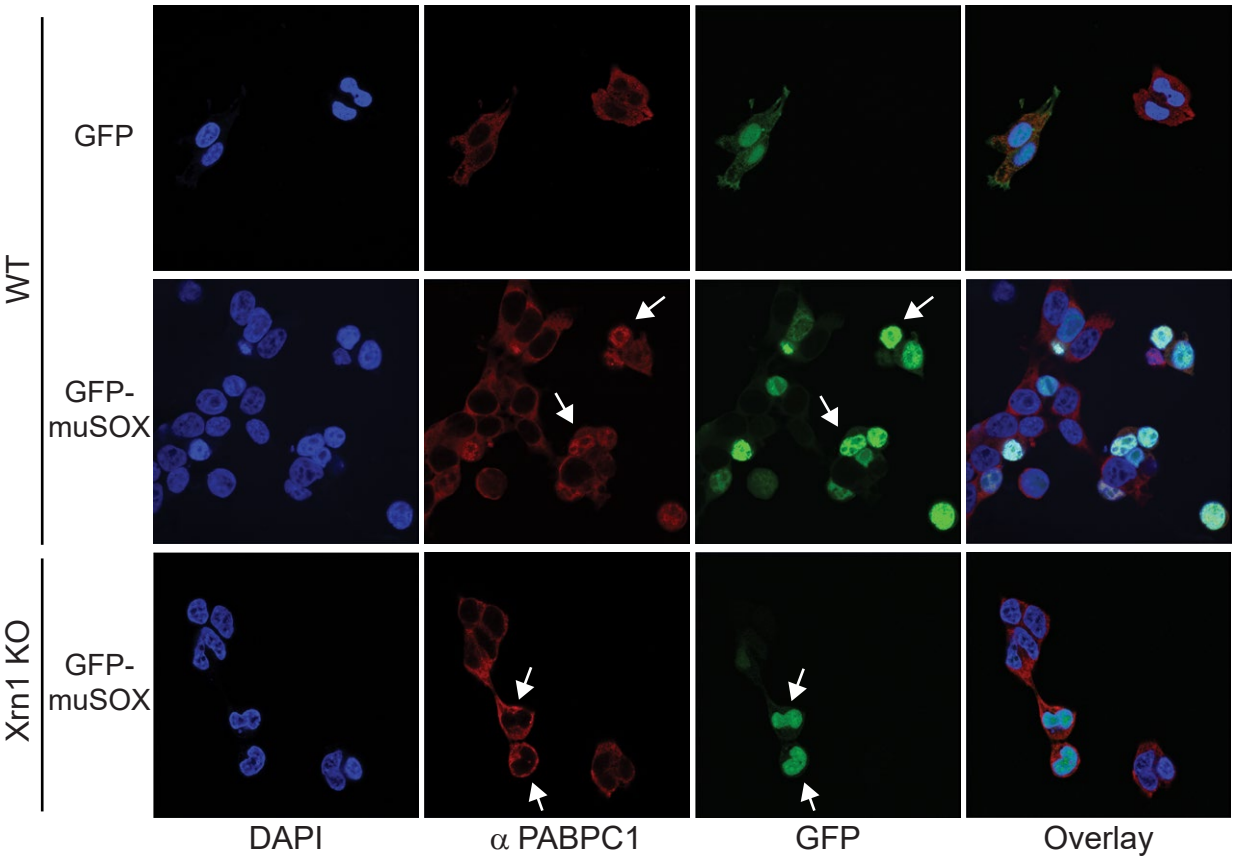

Figure 2. Nuclear translocation of RNA binding proteins is dependent on mRNA degradation by Xrn1. (A) Pie chart showing the percent of shuttling proteins that fail to relocalize in Xrn1 KO cells. (B) Heat map depicting the average nuclear abundance in WT or Xrn1 KO 293T cells of the 67 significantly shifted proteins in samples expressing muSOX or D219A, relative to the empty vector control. (C) Western blots of nuclear, cytoplasmic, and whole cell fractions of WT (left panel) or Xrn1 KO (right panel) 293T cells transfected with the indicated plasmid. GAPDH and HISTONE H3 serve as fractionation and loading controls. (D) Confocal microscopy of WT or Xrn1 KO 293T cells transfected with GFP or GFP-muSOX, showing signals for DAPI stained nuclei (blue), PABPC1 (red), GFP (green), and the merged images (overlay). Arrow heads point to representative GFP-muSOX expressing cells.

Figure 3

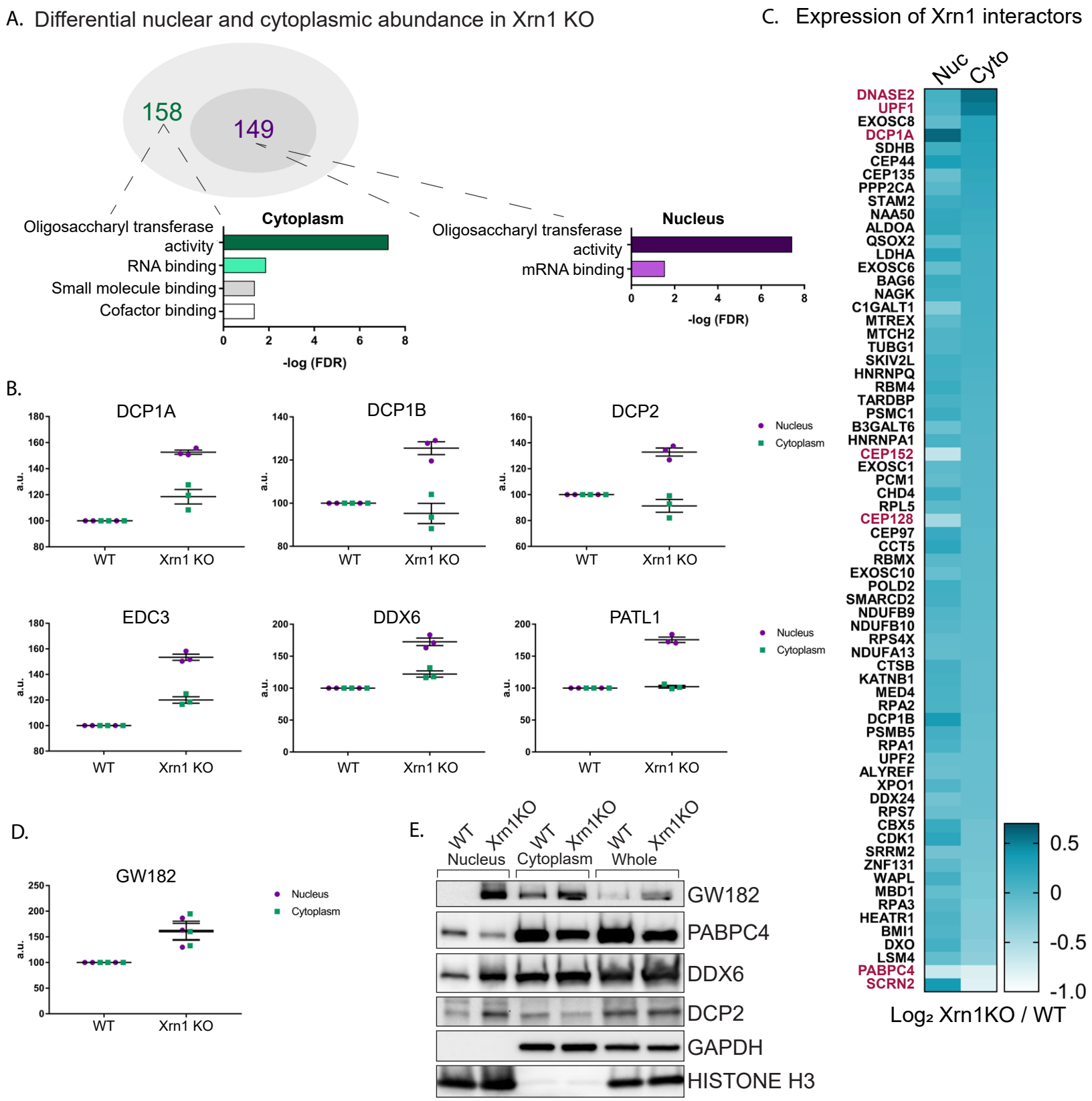

Figure 3. Xrn1 knockout leads to subcellular redistribution of proteins functionally associated with RNA. (A) The number of proteins that are differentially expressed in Xrn1 knockout (KO) cells from the nucleus (149) and the cytoplasm (158). Gene ontology molecular function overrepresentation analysis by Pantherdb is shown for each compartment, graphed according to their false discovery rate (FDR). (B) Graphs showing the nuclear and cytoplasmic distribution of decapping-related proteins from the TMT-MS data. Graphs display the mean with SEM of 3 biological replicates. (C) Heatmap depicting the Log_2 abundance ratio in Xrn1 KO 293T cells compared to WT 293T cells of proteins identified as Xrn1 interactors using the BioGRID database. Proteins with a significant difference in abundance between WT and Xrn1 KO are listed in red. (D) Graph of nuclear and cytoplasmic distribution of GW182 from the TMT-MS data. Graph displays the mean with SEM of 3 biological replicates. (E) Western blot of nuclear, cytoplasmic, and whole cell fractions of WT and Xrn1 KO 293T cells. GAPDH and HISTONE H3 serve as fractionation and loading controls.

Figure 4

A. STRING interaction networks among shuttling proteins

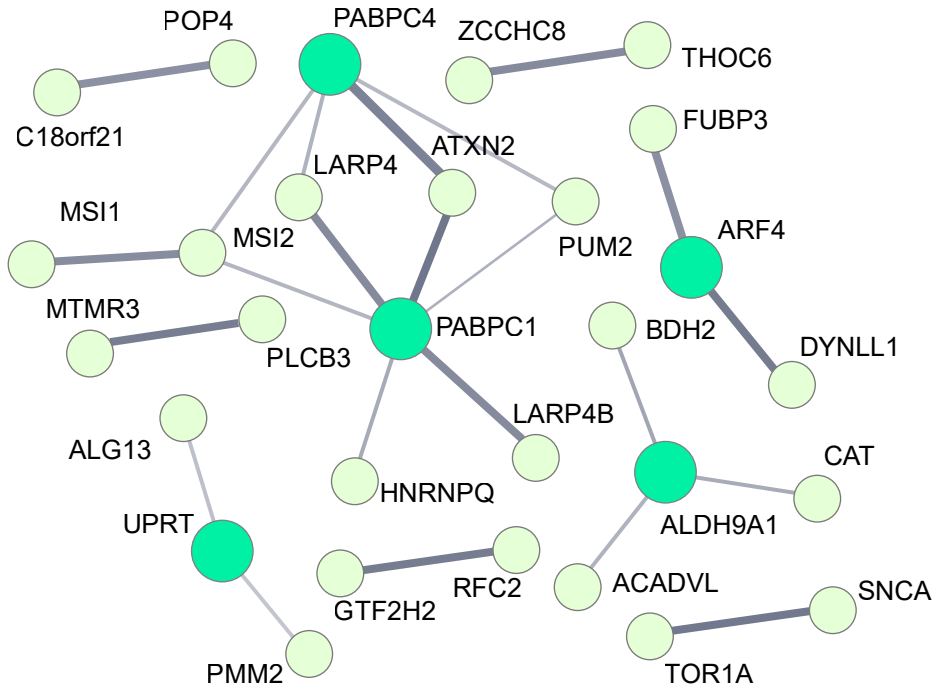

B.

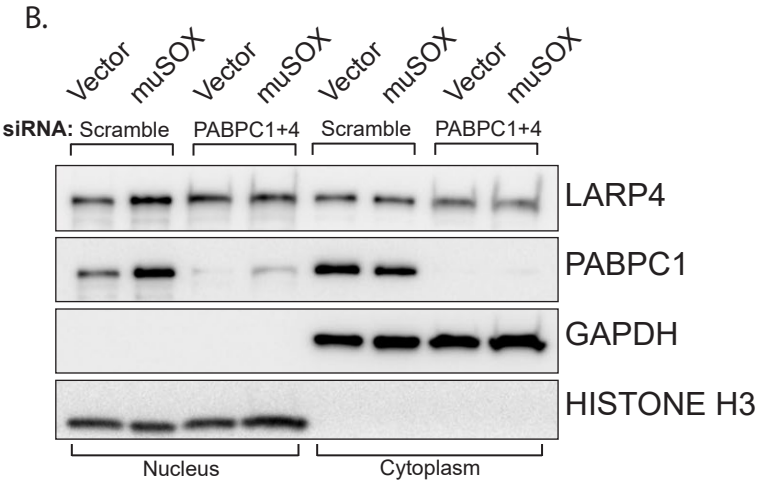

C.

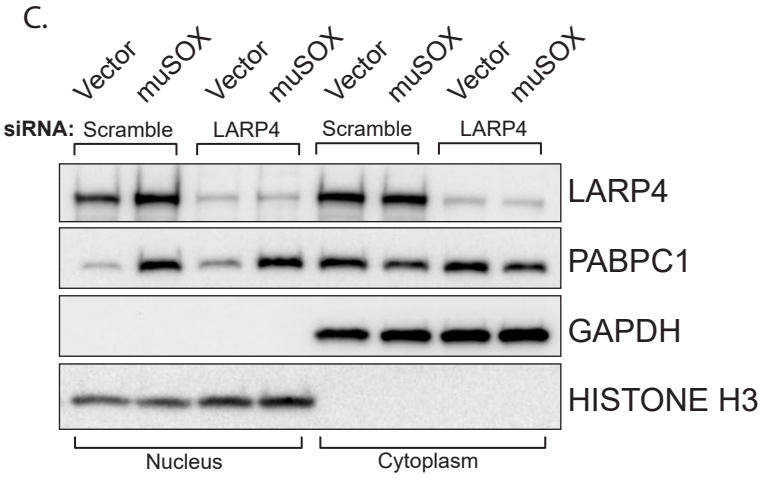

LARP4 Nuclear Quantification

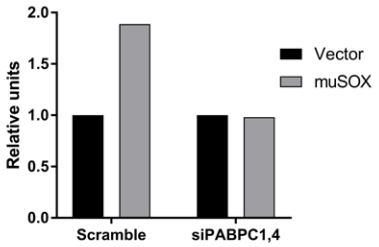

PABPC1 Nuclear Quantification

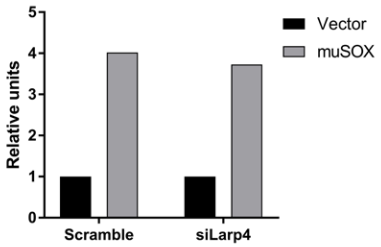

Figure 4. LARP4 translocates to the nucleus in a PABPC-dependent manner. (A) STRING network of reported protein-protein interactions between the 67 proteins that shuttle in muSOX-expressing cells. Medium and high confidence interactions are shown with thin and thick connector lines, respectively. (B, C) Western blots of nuclear and cytoplasmic fractions of vector- or muSOX-transfected 293T cells treated with the indicated siRNA. GAPDH and histone H3 serve as fractionation and loading controls. Quantification of LARP4 and PABPC1 abundance in the nuclear fractions is shown below.

Figure 5

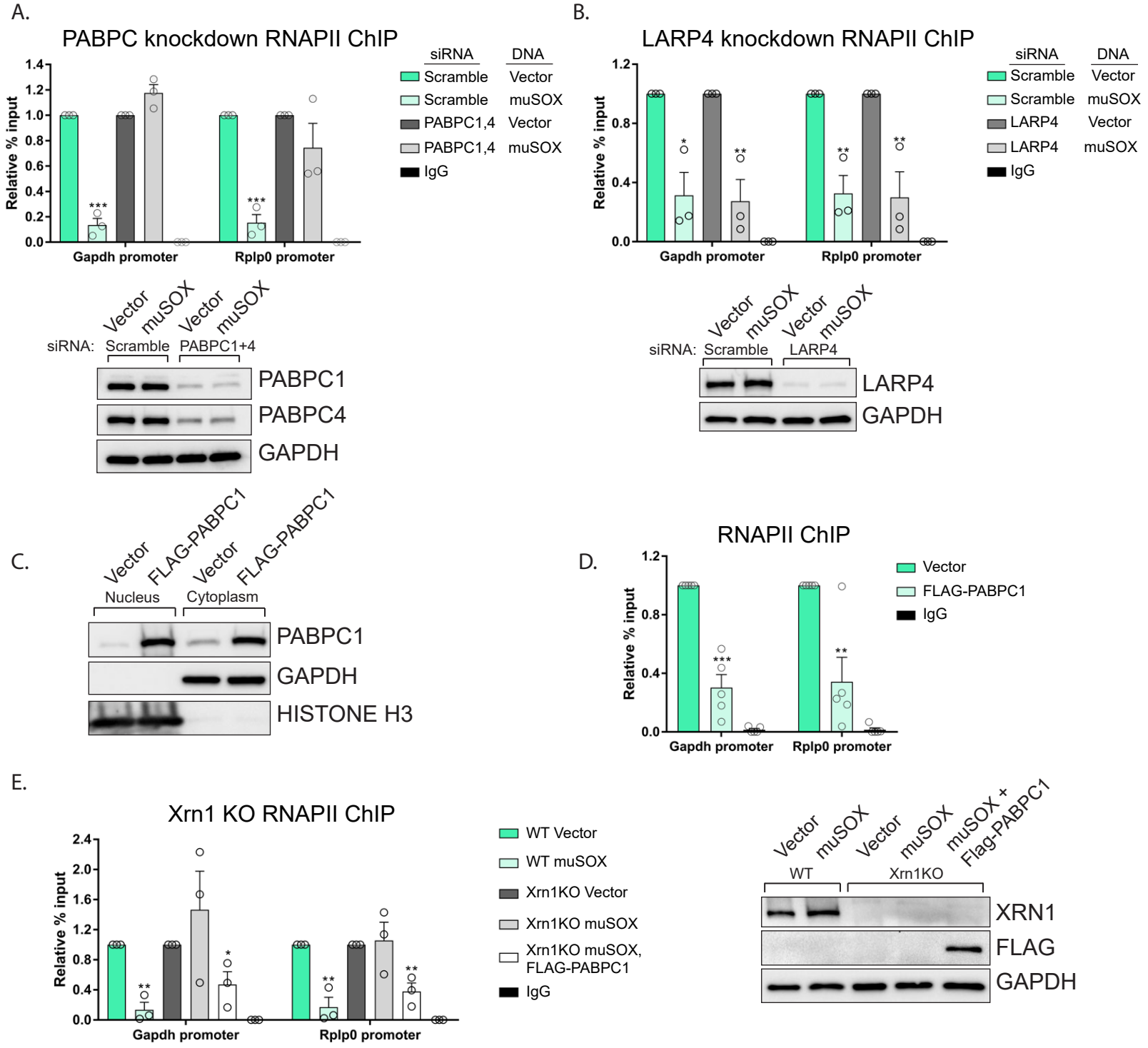

Figure 5. PABPC is required for the connection between mRNA decay and RNAPII transcription.
(A, B) 293T cells treated with siRNAs targeting PABPC 1 and 4 (A), LARP4 (B), or non-targeting scramble siRNAs were subsequently transfected with either empty vector or muSOX, then subjected to chromatin immunoprecipitation (ChIP) using antibodies to RNAPII or IgG. Western blots showing protein levels of PABPC1, PABPC4, and Larp4 after siRNA depletion are shown in the lower panels, along with a GAPDH loading control. (C) Western blots of nuclear and cytoplasmic fractions of 293T cells transfected with an empty vector or a plasmid containing FLAG-PABPC1. GAPDH and histone H3 serve as fractionation and loading controls. (D) 293T cells transfected with either empty vector or FLAG-PABPC1 were subjected to ChIP using antibodies to RNAPII or IgG. (E) WT or Xrn1 KO 293T cells transfected with either empty vector or FLAG-PABPC1 alone or together with muSOX were subjected to ChIP using antibodies to RNAPII or IgG. Purified chromatin in each of the above experiments was quantified by qPCR. Western blots showing the levels of Xrn1 in WT or Xrn1KO 293Ts are shown, along with a GAPDH loading control. All graphs display individual biological replicates as dots, with the mean and SEM. Statistical significance was determined using Student's t test *p <0.05 **p <0.005 ***p <0.0005.

Supplemental Figure 1

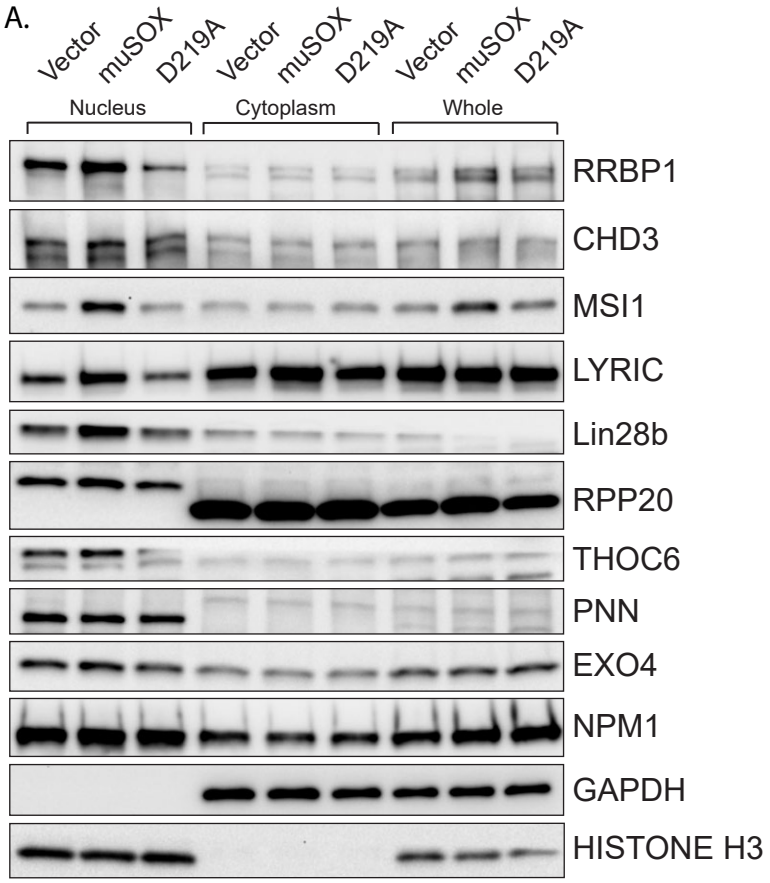

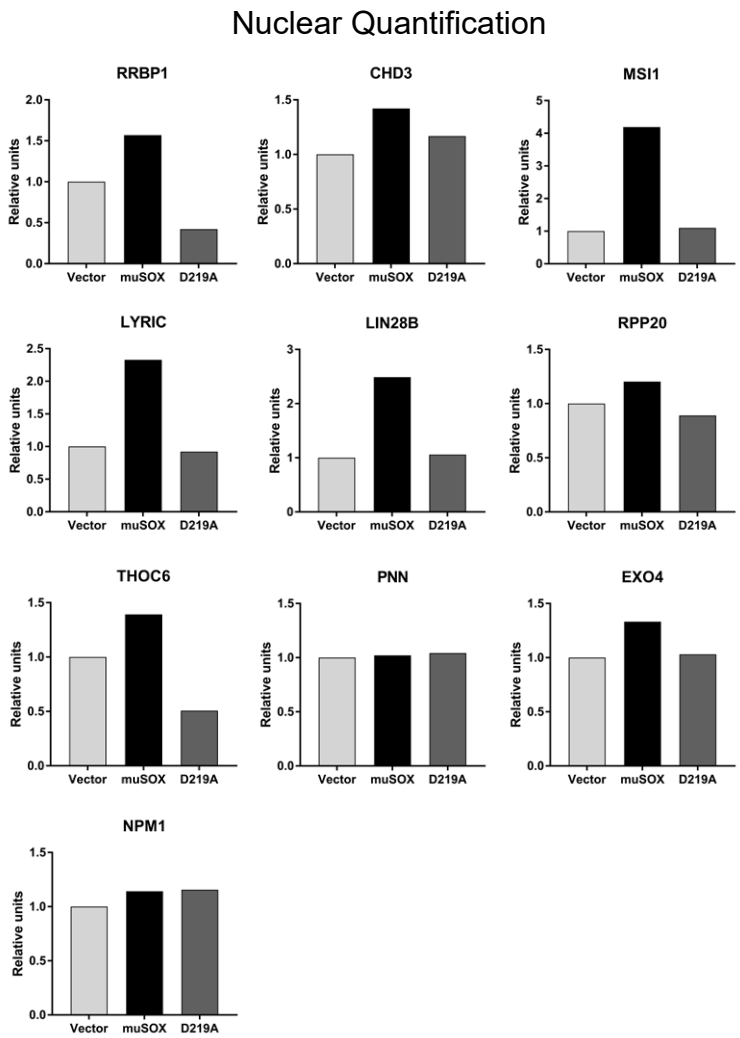

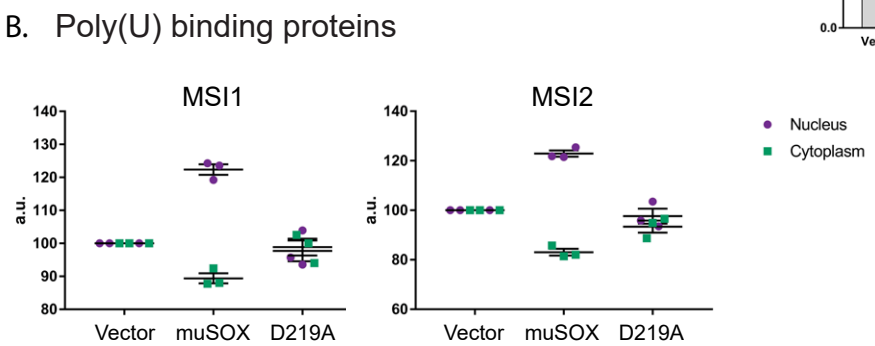

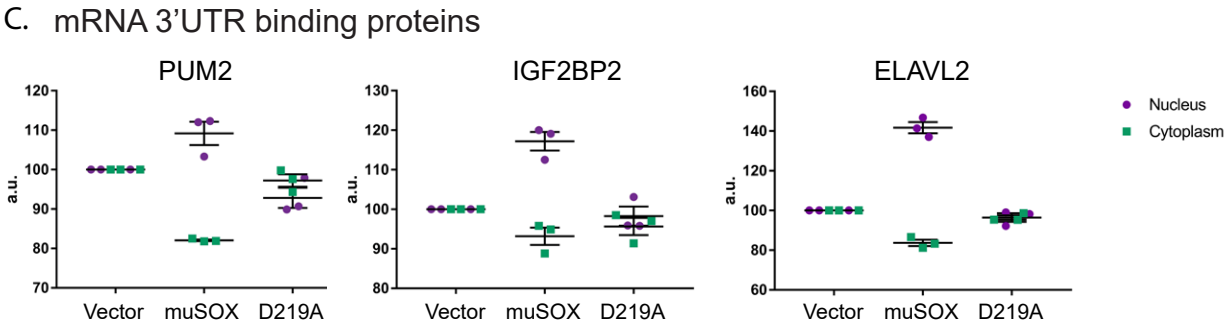

Figure S1 related to Figure 1. RNA binding proteins are translocated from the cytoplasm to the nucleus in cells undergoing enhanced mRNA decay. (A) Western blots of nuclear, cytoplasmic, and whole cell fractions of 293T cells transfected with either empty vector control, WT muSOX, or D219A muSOX. GAPDH and histone H3 serve as fractionation and loading controls. Quantification of the nuclear abundance of each protein is shown on the right. (B, C) Graphs showing poly(U) (B) and 3' UTR (C) binding protein distributions in the nucleus and cytoplasm from the TMT-MS data. Graphs display the mean with SEM of 3 biological replicates.

Supplemental Figure 2

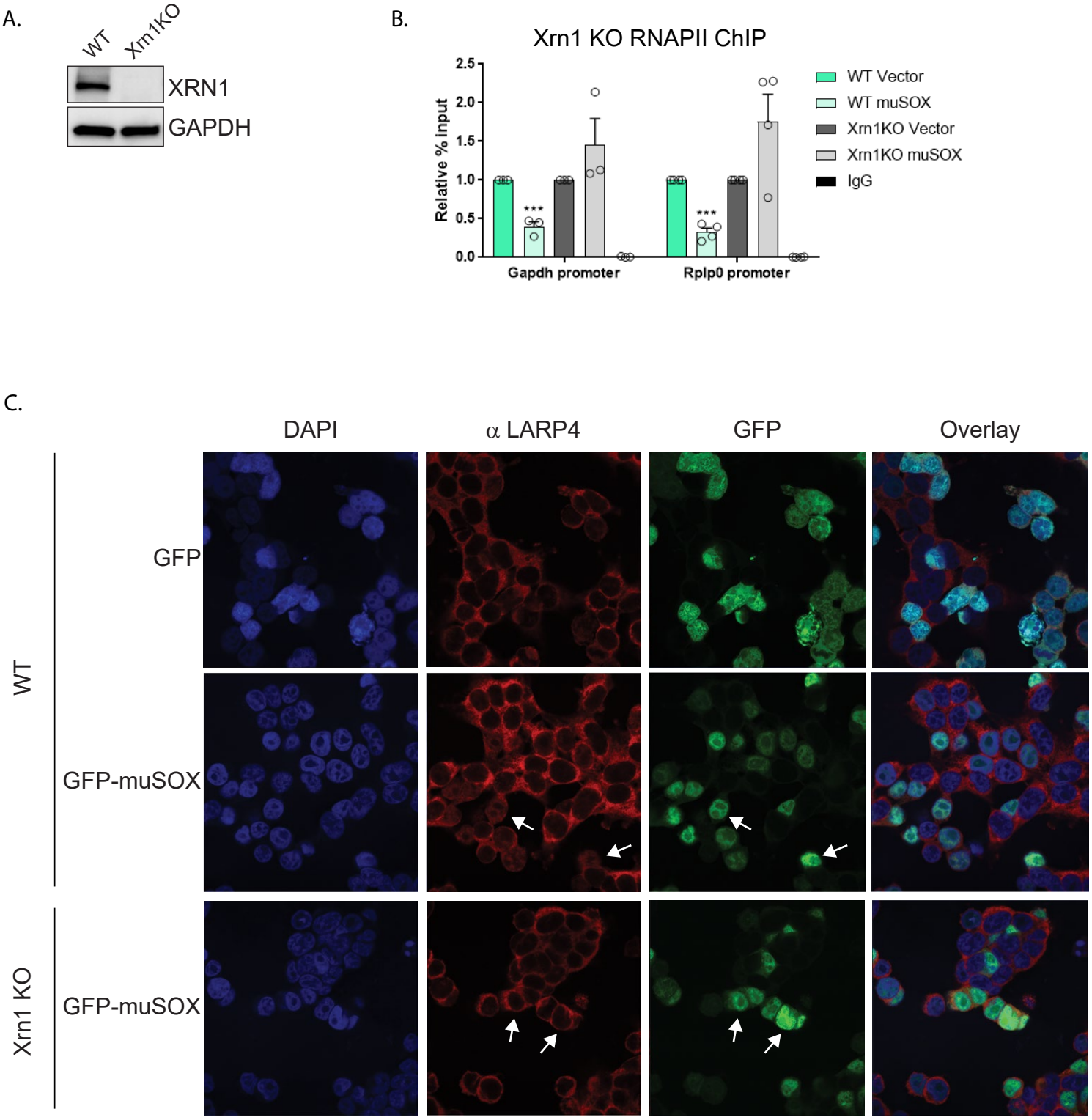

Figure S2 related to Figure 2. Nuclear translocation of RNA binding proteins is dependent on mRNA degradation by Xrn1. (A) Western blots showing the levels of Xrn1 or the GAPDH loading control in WT or Xrn1 KO 293T cells. (B) WT or Xrn1 KO 293T cells transfected with either empty vector or muSOX were subjected to ChIP using antibodies to RNAPII or IgG. Purified chromatin was quantified by qPCR. Graphs display individual biological replicates as dots, with the mean and SEM. Statistical significance was determined using Student's t test *p <0.05 **p <0.005 ***p <0.0005. (B) Confocal microscopy of WT or Xrn1 KO 293T cells transfected with GFP or GFP-muSOX, showing signals for DAPI stained nuclei (blue), LARP4 (red), GFP (green), and the merged images (overlay). Arrow heads point to representative GFP-muSOX expressing cells.

Supplemental Figure 3

OST complex

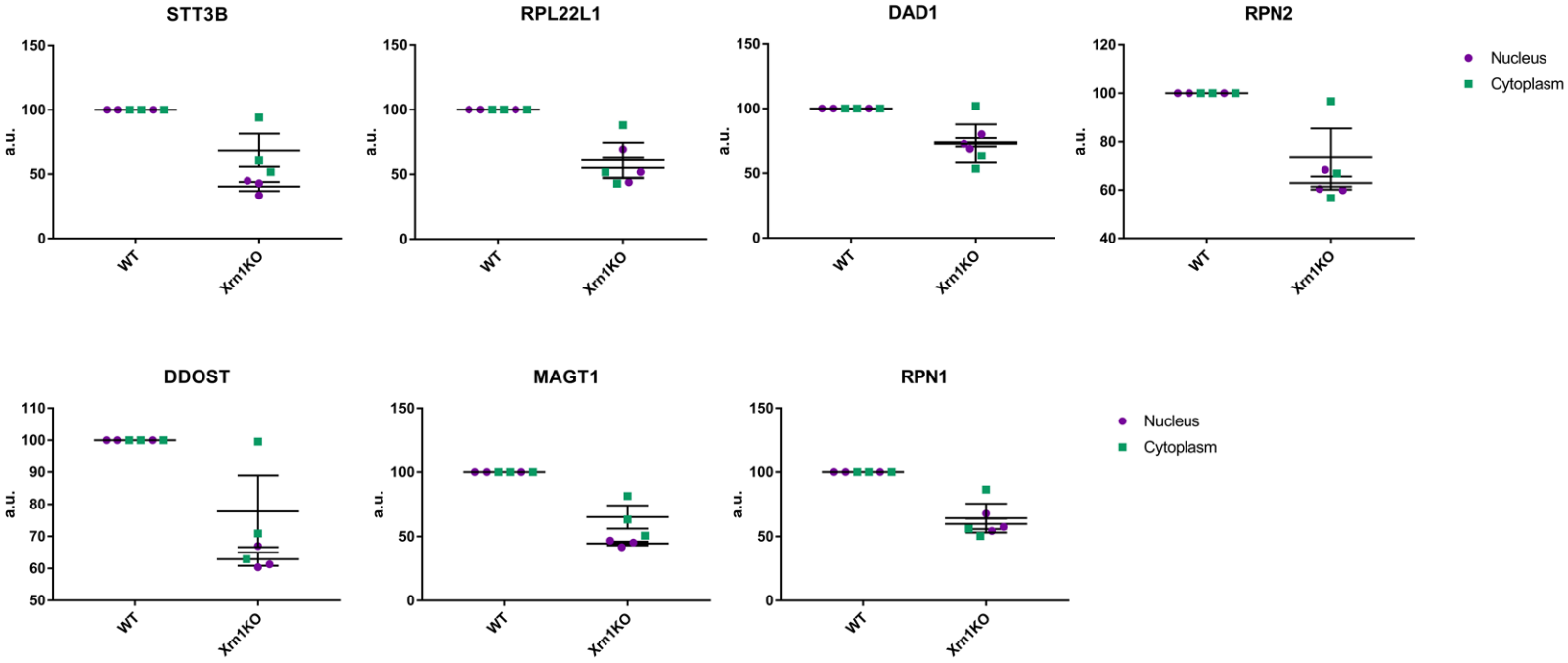

Figure S3 related to Figure 3. Xrn1 knockout leads to subcellular redistribution of proteins functionally associated with RNA. (A) Graphs showing the distribution of proteins of the oligosaccharyltransferase (OST) complex in the nucleus and cytoplasm from the TMT-MS data. Graphs display the mean with SEM of 3 biological replicates.

Supplemental Figure 4

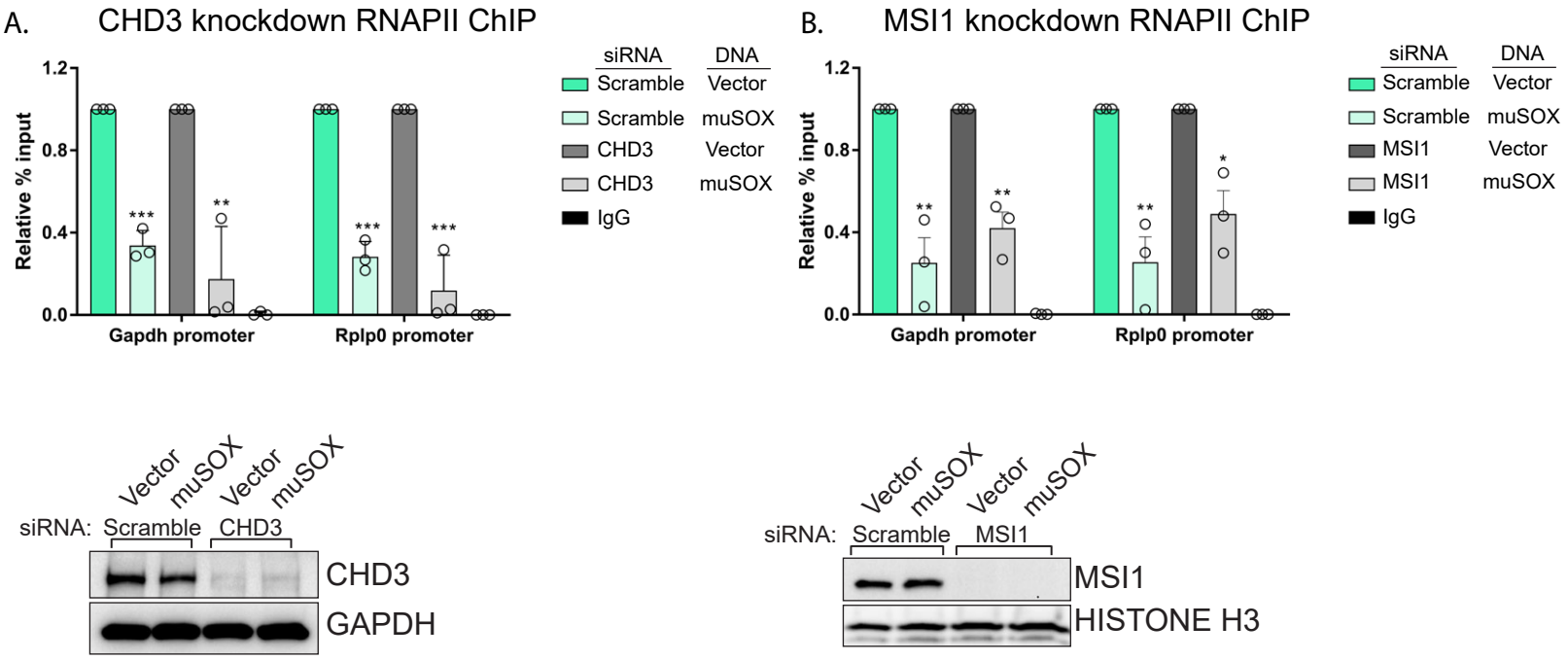

Figure S4 related to Figure 5. PABPC is required for the connection between cytoplasmic mRNA decay and RNAPII transcription. (A, B) 293T cells were treated with siRNAs targeting CHD3 (A), or MSI1 (B), or non-targeting scramble siRNAs, then transfected with either empty vector or muSOX and subjected to chromatin immunoprecipitation (ChIP) using antibodies to RNAPII or IgG. Purified chromatin was quantified by qPCR. Western blots showing the levels of CHD3 and MSI1 after siRNA depletion, along with a GAPDH or histone H3 loading control are shown below. Graphs display individual biological replicates as dots, with the mean and SEM. Statistical significance was determined using Student's t test *p <0.05 **p <0.005 ***p <0.0005.